

Electric-field-driven CO₂ polarization and bioinspired proton blocking unlock CO₂ reduction in strong acid without metal cations

Received: 21 September 2024

Accepted: 7 January 2026

Published online: 19 January 2026

Check for updates

Liwei Chen^{1,7} , Zhenbin Guo^{2,7}, Hui-Zi Huang², Wenjing Tian², Xiaoxue Chang², Qiang Hu³, Di Liu⁴, Chao Sun², Mingming Gao¹, Suqin Han¹, Shuhua Lv¹, Huiqin Zhou⁵, Linyu Hu⁶, Hongyu Mou¹, Xing Gao¹, Yuchen Hao^{1,3} , Wenxiu Yang², Qunsheng Li⁵ , Bo Wang² & Jibin Song⁵

Metal-cation-free CO₂ electroreduction (CO₂R) in strong acidic media mitigates CO₂ reactant losses, eliminates the risk of metal salt precipitation, and broadens device tolerance compared to acidic, neutral, or alkaline system using metal cations. However, such an acidic environment still poses challenges due to the inert and nonpolar nature of CO₂ and intensely competitive hydrogen evolution reaction. Inspired by aquaporins in acidophiles, we engineer sharp-triangle Au nanostructures capped with a hexadecyltrimethylammonium chloride (CTAC) layer enriched with cationic sites. The intense local electric fields generated by the high-curvature tips of Au nanocatalyst polarize CO₂ molecules, increasing their dipole moment to facilitate adsorption and activation. Meanwhile, the CTAC layer acts as a proton barrier, suppressing HER by mimicking the proton-blocking mechanism of aquaporins. This dual-function design enables continuous CO₂R for 100 hours in a flow electrolyzer at pH 1.0, achieving an energy efficiency of 60% and near-unity Faradaic efficiency for CO production. This bioinspired strategy represents a significant advancement in CO₂R technology by integrating rational catalyst design principles.

Electrochemical reduction of CO₂ in ambient conditions is a promising technique for storing renewable electricity, fixing CO₂, and producing value-added fuels and chemicals^{1,2}. Among the various approaches, performing CO₂R in an acidic medium is particularly attractive for efficient CO₂ utilization due to its potential to avoid the formation of

carbonates^{3,4} that typically occur in alkaline^{5,6} and near-neutral^{3,7,8} electrolytes. However, efficient and selective CO₂R in acidic conditions remains a challenge due to the competitive hydrogen evolution reaction (HER) and the inert nature of the CO₂ molecule^{9–18}. Introducing high concentrations of alkali cations into the electrolyte, even utilizing

¹College of Biological and Chemical Engineering, Qilu Institute of Technology, Jinan, P. R. China. ²Ministry of Education Key Laboratory of Cluster Science, Beijing Key Laboratory of Photoelectronic/Electrophotonic Conversion Materials, Analysis and Testing Center, Frontiers Science Center for High Energy Material, Advanced Technology Research Institute (Jinan), School of Chemistry and Chemical Engineering, Beijing Institute of Technology, Beijing, P. R. China. ³Research Center for Solar Driven Carbon Neutrality, School of Physics Science and Technology, Institute of Life Science and Green Development, Hebei University, Baoding, P. R. China. ⁴Department of Pharmaceutical Engineering, School of Life and Health Sciences, Huzhou College, Huzhou, P. R. China. ⁵State Key Laboratory of Chemical Resource Engineering, College of Chemistry, College of Chemical Engineering, Beijing University of Chemical Technology, Beijing, P. R. China. ⁶College of Physics, Sichuan University, Chengdu, P. R. China. ⁷These authors contributed equally: Liwei Chen, Zhenbin Guo.

e-mail: chenliwei@qlit.edu.cn; haoyc@hbu.edu.cn; liqs@mail.buct.edu.cn; bowang@bit.edu.cn; jibin.song@buct.edu.cn

the tip effect to enrich alkali metal ions on the catalyst surface, has been demonstrated to suppress the undesired HER while promoting CO₂ activation^{9,19,20}. Despite the progress, alkali cations induce bicarbonate crystallization on the catalyst and gas diffusion electrode during CO₂R in the acidic electrolyte, which is still an issue that limits the cell's lifetime^{5,10,11,21–23} and hinders the sustainability of CO₂ reduction^{19,21}.

Acidic electrolytes without metal cations eliminate carbonate formation, enabling high CO₂ utilization efficiency^{9,11,13}. However, the kinetics of CO₂R in such environments inevitably confronts two formidable hindrances: (i) the inherent difficulty in activating the chemically inert and nonpolar CO₂ molecule and (ii) the severe competition from HER at low pH^{9,24–26}, often necessitating high overpotentials and resulting in suboptimal energy efficiency. Interestingly, biological systems like aquaporins in acidophiles can selectively block protons due to the presence of specific positively charged residues of amino acid^{27,28}, suggesting that mimicking such biological mechanisms of the proton-blocking process could provide a means to suppress HER in CO₂R (Fig. 1a, b). Simultaneously, engineering strategies to polarize and activate CO₂ molecules by breaking their nonpolar ground state are essential for improving CO₂ reduction kinetics^{29,30}. Notably, the application of intense local electric fields offers a promising approach to achieve such polarization, providing a viable pathway to overcome the intrinsic challenges of CO₂ activation in metal-cation-free acidic media.

Here, we present that a bioinspired sharp-triangle Au nanocatalyst with the cationic surfactant layer enables efficient and durable CO₂ reduction in a metal-cation-free strongly acidic medium by promoting CO₂ polarization while suppressing competitive HER. For CO₂ activation, simulations reveal tenfold higher local electric fields associated with metallic tips of Au nanotriangles (AuNTs) compared to quasi-spherical electrode regions. The field-induced polarization effect not only enables the CO₂ adsorption process to be thermodynamically spontaneous, but also increases the dipole moment of nonpolar CO₂ (Fig. 1c, d), which in turn elongates the bond length and weakens the bond, lowering the barrier of the rate-determining step (RDS). For inhibition of HER, the positively charged hexadecyltrimethylammonium chloride (CTAC) layer on the Au surface (Fig. 1e) builds on the proton-blocking mechanism of aquaporins (Fig. 1b), allowing electrically neutral CO₂ to pass through while preventing proton transfer. This extended charge distribution on the CTAC layer enhances the proton exclusion effect, further suppressing HER. As a result, the AuNTs catalysts achieve about 60% energy efficiency and a near-unity Faradaic efficiency over 100 h of electrolysis in acidic electrolytes (pH = 1.0), making the CTAC-capped AuNTs one of the most efficient catalysts for acidic CO₂R to date. This work underscores the potential of bioinspired design principles in advancing CO₂R technologies, offering a sustainable pathway for CO₂ utilization in acidic conditions.

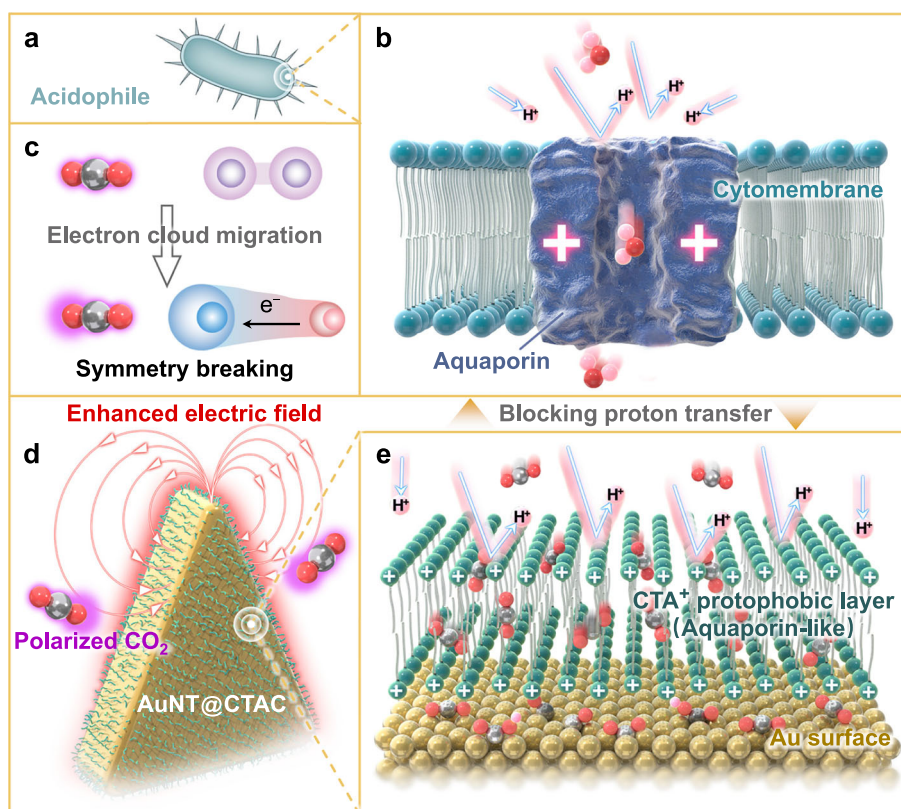


Fig. 1 | Bioinspired nanocatalyst design for efficient CO₂R in acidic media.

a Schematic representation of an acidophile, highlighting the natural proton-blocking mechanism in highly acidic environments. **b** Schematic representation of aquaporins embedded in the cytomembrane. Positively charged residues within the aquaporin channel selectively repel protons while allowing neutral water molecules to pass through. **c** Charge redistribution in a free CO₂ molecule under an external electric field, leading to symmetry breaking and dipole induction. The migration of the electron cloud creates an asymmetric charge distribution, making CO₂ more prone to adsorption and activation. **d** The intense local electric field at the tips of AuNTs capped with CTAC polarizes CO₂ molecules, increasing their dipole moment and facilitating efficient adsorption and activation.

e Representation of the AuNTs surface capped with a CTAC protophobic layer. The cationic CTA⁺ layers distributed across the surface extend the concept of proton repulsion seen in aquaporins, creating a continuous positive charge environment. While this illustration would not reflect direct structural evidence, it highlights the broader proton exclusion zone, which aids in further suppressing HER and enhances the catalyst's effectiveness in CO₂ reduction. Gold spheres represent Au atoms; green spheres and gray tails represent CTA⁺ groups, where the gray hydrocarbon chains correspond to alkyl chains; red, gray, and light pink spheres represent O, C, and H atoms, respectively. The purple halo around CO₂ molecules indicates the distribution of their electron clouds.

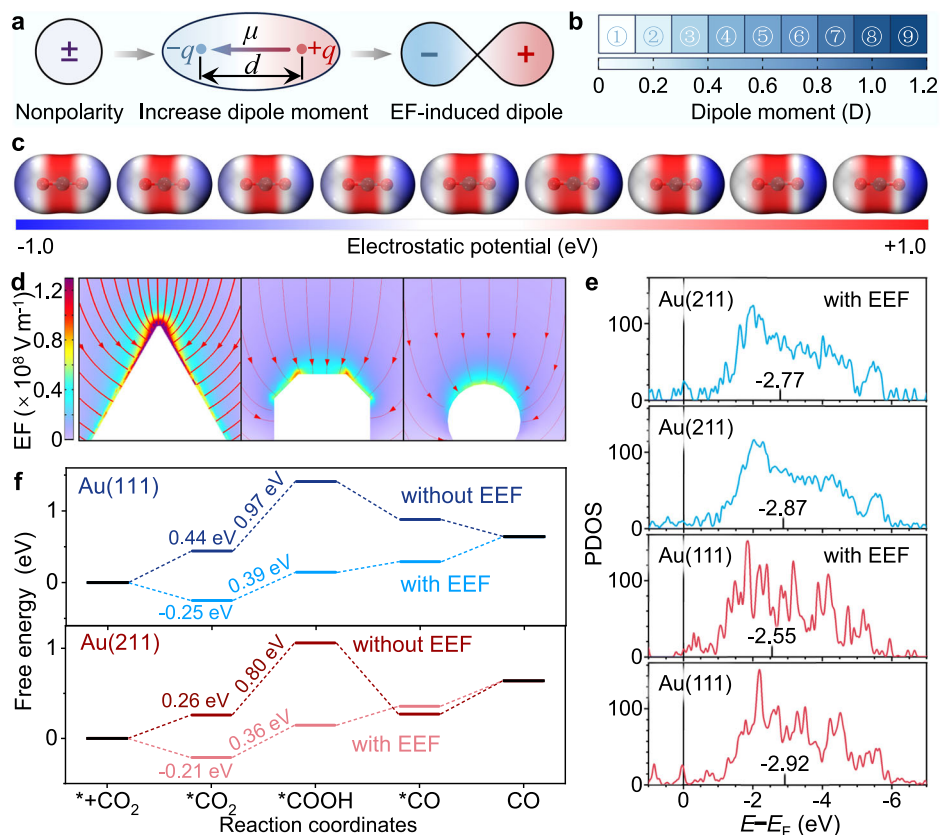


Fig. 2 | Theoretical predictions of CO₂ activation under enhanced electric field.

a Schematic illustration of the transition from nonpolarity to EF-induced dipole for free CO₂ molecules. A dipole moment (μ) forms as the external electric field (EF) shifts the electron cloud, separating charges $+q$ and $-q$ over distance d . **b** Simulation results showing the increase in the dipole moment of free CO₂ molecules as the electric field intensity increases from 0, 0.15, 0.3, 0.45, 0.6, 0.75, 0.9, 1.05 to $1.2 \times 10^8 \text{ V m}^{-1}$. **c** Electrostatic potential maps of free CO₂ molecules under different electric field intensities, indicating the separation of positive and

negative charge centers. **d** COMSOL Multiphysics simulations of the electric field distribution around different Au surface geometries: (left) sharp triangle, (middle) obtuse surface, and (right) round surface, showing the highest field concentration at the sharp triangle tip. **e** Projected density of states (PDOS) for Au(211) and Au(111) facets with and without EEF. **f** Gibbs free energy diagrams for CO₂R on Au(111) and Au(211) facets with and without EEF. The EEF lowers the energy barriers for CO₂ reduction, indicating enhanced adsorption and activation on Au surfaces.

Results

Theoretical predictions

Since the positive and negative charge centers of the free CO₂ molecule with linear structure coincide and the polarity of the bonds cancel each other out, it is a nonpolar molecule with a dipole moment of 0 D. We firstly focus on the CO₂ molecule approaching the catalyst surface, before any chemical interaction with Au occurs. Under these conditions, CO₂ retains its linear structure, as there is no charge transfer or bonding with the surface to induce bending^{31–33}. Through theoretical calculation simulation (Fig. 2a–c), we discovered that the external electric field could break the nonpolar state of the CO₂ molecule, shift and deform its electron cloud, separate positive and negative charge centers, and produce an induced dipole. A dipole is defined as a pair of opposite charges $+q$ and $-q$ separated by a distance d (Fig. 2a). The direction of the dipole moment (μ) in space is from negative charge $-q$ to positive charge $+q$ ³⁴. The CO₂ dipole moment, bond length, and bond energy of C=O was highly dependent on the electric field intensity. Specifically, one of the C=O bond energy is declined, bond lengths is increased gradually from 1.169 to 1.182 Å (Supplementary Fig. 1) with the corresponding dipole moment of CO₂ molecules elevated from 0 to 1.25 D (Fig. 2b) when the electric field intensities are raised from 0 to $1.2 \times 10^8 \text{ V m}^{-1}$, respectively. That is, the higher the electric field strength, the larger the CO₂ dipole moment and the weaker the C=O bond. According to the electrostatic potential (ESP) diagram for CO₂ molecules under different electric fields in Fig. 2c, higher polarizability of CO₂ molecules under a stronger electric

field could be ascribed to a higher separation degree of positive and negative charge centers as well as increased charge under stronger electric fields.

As high-curvature structures are known to concentrate electric fields that can affect the spatial distribution of charged or polarizable species³⁵. Under an applied potential, metallic electrodes tend to accumulate free electrons at surface regions with pronounced curvature, leading to locally intensified electrostatic fields. This field enhancement arises from curvature-dependent electron redistribution inherent to charged metal surfaces³⁶. We used COMSOL Multiphysics simulations with a finite-element numerical method^{37–39} to explore the prospects of tip-enhanced field intensification (Fig. 2d) and the associated field distribution (Supplementary Fig. 2) on Au surface with various acutance. As the tip geometry sharpens from round to triangular, the simulated electric field intensity (Fig. 2d) near the surface increases by roughly one order of magnitude, reaching up to $1.21 \times 10^8 \text{ V m}^{-1}$ at the CO₂/CO equilibrium potential (-0.109 V versus standard hydrogen electrode). Under such intensified fields, a polarized CO₂ molecule is expected to orient such that its electropositive end faces the high-field region (Supplementary Fig. 2). These results illustrate the effective ability of sharp angles to enhance the electric field, which may promote near-surface polarization and retention of CO₂ molecules.

We employed density functional theory (DFT) calculations (Supplementary Data 1) to predict further the adsorption and electrocatalytic conversion of CO₂ on typical Au facets—flat Au(111) plane and

the stepped Au(211) facet—with/without the enhanced electric field (EEF). The surface electronic structures of the Au nanocrystals would be significantly altered by the applied EEF⁴⁰. The *d*-band centers of the Au(111) and Au(211) planes under the EEF of $1.21 \times 10^8 \text{ V m}^{-1}$ were clearly shifted upward by 0.37 and 0.10 eV, respectively, compared with those without the EEF (Fig. 2e). Based on the basic concepts of surface and coordination chemistry, an upward movement of the outermost *d*-band center in transition metals raises a greater fraction of anti-bonding orbitals above the Fermi energy. This reduces the occupation of anti-bonding states, thereby reinforcing the interaction between the metal surface and adsorbed species, such as CO₂ and its intermediates⁴¹. In the case of CO₂R, the Au surface atoms under the EEF would bond with the adsorbates (e.g., *CO₂, *COOH) much more strongly than those without the EEF due to their upshifted 5*d* bands⁴¹. Enhancing adsorption on Au surfaces would theoretically promote CO₂R since Au showed relatively weak adsorption to CO₂ species^{42–44} and key intermediates (such as *COOH) and was located on the right side of the volcano plot for CO₂R^{1,45}. While these results highlight the role of the *d*-band center shift in modulating CO₂ adsorption, it is also crucial to consider the dipole-field interaction between CO₂ and the electric field. As suggested by the dipole-field model^{46,47}, the strong dipole moment of CO₂ interacts with the interfacial electric field, further stabilizing the adsorbed *CO₂. Our findings are consistent with this model, as we observe significant C–O bond elongation (from 1.182 to 1.354 Å on Au(111) and to 1.361 Å on Au(211)) and O–C–O bond bending (from 179.6° to 124.3° on Au(111) and 122.7° on Au(211)), both of which are indicative of strong electrostatic interactions. Bader charge analysis further revealed electron transfer from C to O (−0.218 e on Au(111) and −0.302 e on Au(211)), indicating that CO₂ activation occurs through both geometric and electronic structural changes. These structural changes suggest that the observed enhancement in CO₂ adsorption is not solely attributed to the *d*-band shift, but also to the polarization of CO₂ under the EEF, in agreement with the dipole-field model.

Further evidence was provided by the DFT-calculated Gibbs free energy (ΔG) diagrams for CO₂R on different Au facets models at 298 K and 1 atm (Fig. 2f and Supplementary Figs. 3 and 4). Notably, the Au surfaces with the EEF exhibited significantly strengthened CO₂ adsorption, which is the first critical step for subsequent catalytic reactions^{1,41}. The free energy of CO₂ adsorption on the (111) and (211) facets was 0.44 and 0.26 eV, respectively. But, under the EEF, the CO₂ adsorption on the Au surface transforms into a thermodynamic spontaneous process, and its free energy changes decrease to −0.25 and −0.21 eV, respectively. In addition, the EEF modulates the CO₂ reduction process and lowers the thermodynamic energy barrier of CO₂R for all typical Au facets. On the Au(111) plane, the EEF stabilizes the rate-determining *COOH and *CO intermediates^{38,45} by 0.14 eV and 0.29 eV, respectively, similar to the under-coordinated Au(211) facet (Fig. 2f). These findings emphasize that the combination of enhanced CO₂ adsorption and intermediate stabilization under EEF conditions potentially contributes to the improved catalytic performance of Au nanostructures for CO₂R. Especially, the Au facets under the EEF would share a similar potential-determining step (PDS) for CO₂R (i.e., *CO₂ + H⁺ + e[−] → *COOH) that not under the electric field, but with much lower energy barriers of 0.39 and 0.36 eV, respectively. This reduction in energy barriers corresponds to a significant decrease in the overpotential by 580 and 440 mV for Au(111) and Au(211) facets, respectively. Such a decrease demonstrates the effectiveness of the EEF in facilitating the rate-determining step and enhancing the overall catalytic performance of CO₂ reduction. Therefore, the much lower free energy requirement would suggest the boosted CO₂ adsorption and reduction on the surface under the EEF. These findings emphasize that CO₂ activation under the EEF is governed by multiple factors, and its underlying mechanisms can be described using different descriptors. Notably, in our DFT models, the adsorbed *CO₂ species

represents a field-stabilized, weakly chemisorbed precursor state prior to the first electron transfer, rather than a fully reduced *CO₂[−] radical. The pronounced geometric bending and charge redistribution observed under the applied electric field indicate partial electron transfer and polarization, which effectively mimic the early stage of CO₂ activation (CO₂ → CO₂[−]) at the electrode interface. In addition to the *d*-band center shift, which alters the electronic structure of the catalyst, the dipole-field interaction plays a crucial role in stabilizing adsorbed CO₂ via electrostatic polarization. Moreover, the adsorption energy of CO₂ serves as a fundamental descriptor for catalytic activity, as stronger CO₂ binding often correlates with enhanced reactivity. Finally, the local electric field effects, which modulate the adsorption and reaction energetics of key intermediates, further influence the catalytic performance. These descriptors collectively highlight the considerable potential of Au nano-angle with EEF in boosting CO₂ adsorption and activation⁴⁸. DFT calculations provide qualitative insight, though real catalytic conditions may involve additional complexities beyond the present model. Collectively, these findings establish a dual electric field effect—that is, a two-stage manifestation of the same electric field, where the external field first polarizes and enriches approaching CO₂ molecules in the pre-adsorption regime, while the interfacial field subsequently stabilizes the adsorbed intermediates and lowers reaction barriers in the post-adsorption regime, forming a continuous field-mediated activation pathway.

Synthesis and characterizations of Au nanostructures

To probe experimentally the predictions, we used growth-purification process as a convenient and scalable means of preparing desired Au-catalysts of nanoparticle with obtuse-angle surface and high-curvature nanotriangle with acute-angle surface.

The experimental approach for synthesizing AuNTs involves two steps (see “Materials and Methods”): the nanocrystal growth process⁴⁹ and the product purification⁵⁰. In a typical experiment, CTAC as the surfactant was first mixed with potassium iodide, followed by the addition of sodium tetrachloroaurate solution. When ascorbic acid is introduced, Au(III) species are promptly reduced to Au(I), which can be visually confirmed by the fading of the solution’s yellow hue to nearly colorless. Subsequently, the swift addition of NaOH triggers the further reduction of Au(I), resulting in the nucleation and growth of AuNTs⁴⁹. To isolate Au nanotriangles free from quasi-spherical impurities, we employed a purification route based on controlled aggregation and precipitation. The shape-selective separation occurs through depletion-induced attractions among particles in the CTAC micellar medium. These forces emerge when the interparticle gap becomes smaller than the effective size of the micelles acting as the depleting species⁵⁰. This approach presents two crucial benefits: the stability of the AuNTs is not compromised at high CTAC concentrations, and centrifugation is not necessary due to the nature of the CTAC stock solution. In addition, when cetyltrimethylammonium halide is used, a surfactant bilayer on gold nanostructures has been evidenced⁵¹. The removal of residual isotropic particles was visually evident from the gradual color transition of the colloid from deep blue to indigo. Spectroscopically, this purification is reflected by a marked decrease in the 520–530 nm plasmon band associated with isotropic species⁵⁰, while the characteristic dipolar resonance of AuNTs remained dominant (Supplementary Fig. 5). Transmission electron microscopy (TEM) analysis confirmed the separation of NTs: the supernatant mainly comprised different quasi-isotropic particles (Supplementary Fig. 6), while the high-purity level of NTs was in the precipitate (Supplementary Fig. 7 and Fig. 3a–d).

The blue colloidal solution was obtained by redisperse precipitation with water (inset of Fig. 3e). As displayed in Fig. 3e, the resulting Au nanoplates exhibit a pronounced plasmonic resonance peak centered near 655 nm and a minor shoulder around 570 nm, corresponding to the in-plane and out-of-plane dipolar resonance,

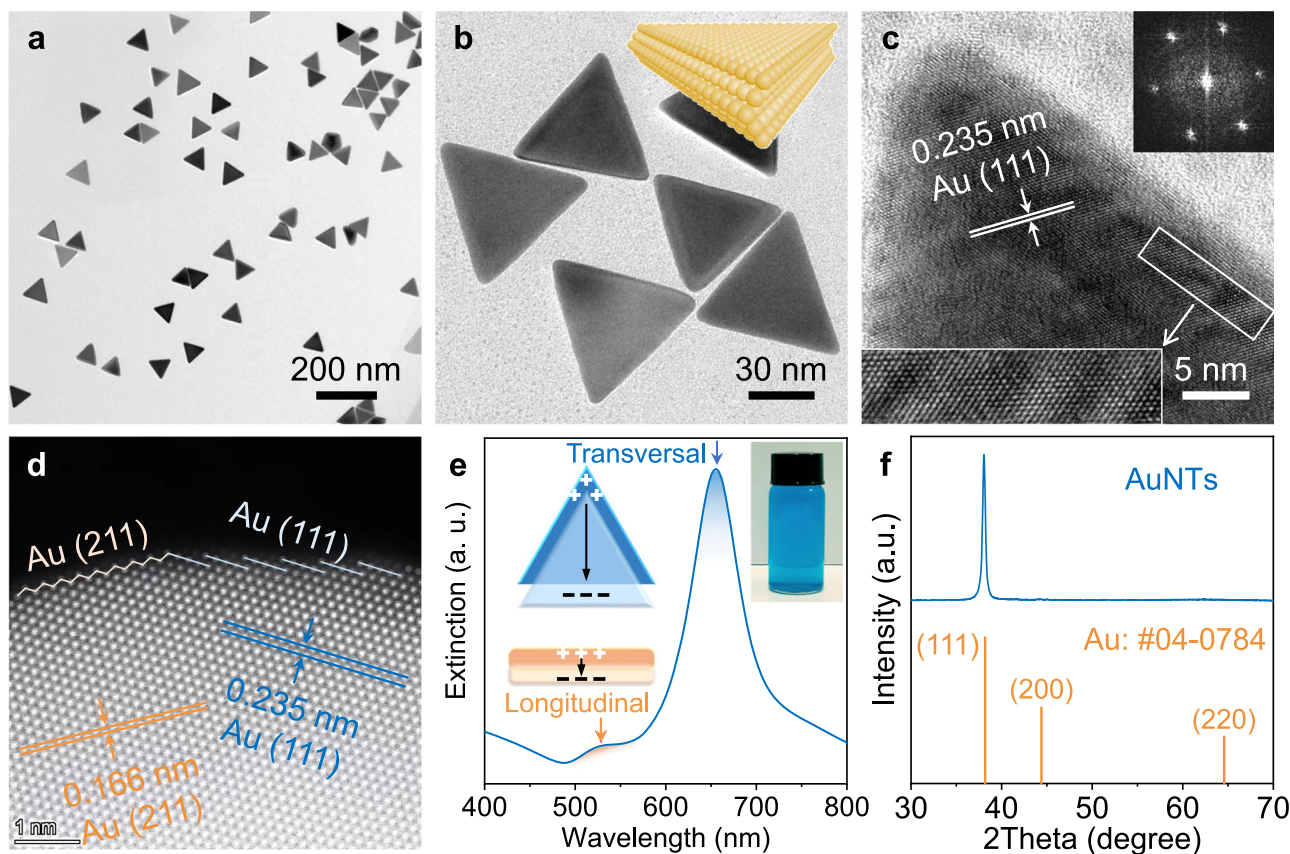


Fig. 3 | Characterization of AuNTs. **a** TEM image. **b** Higher magnification TEM image. The inset illustrates the structure of the AuNTs. **c** HRTEM image showing the lattice fringes of AuNTs. The inset displays the corresponding FFT pattern, confirming the single-crystalline nature of the AuNTs with a (111) plane. **d** AC-HAADF-

STEM image highlighting the (111) basal planes and (211) stepped facets of AuNTs. **e** Extinction spectra of AuNTs with the inset showing the blue colloidal solution. The peaks correspond to in-plane (655 nm) and out-of-plane (570 nm) dipole resonances. **f** XRD pattern of AuNTs.

respectively⁴⁹. The absence of a characteristic resonance around 520–530 nm indicates a predominance of anisotropic nanostructures, consistent with the TEM observations. The edge length distribution of the monodispersed AuNTs with sharp tips was 67.30 ± 3.29 nm (Supplementary Fig. 7). High-resolution TEM (HRTEM) images and X-ray diffraction (XRD) patterns suggested that the planar facet was the (111) facet (Fig. 3c and f). The corresponding fast Fourier transform (FFT) pattern taken from the middle area of a nanostructure in the inset of Fig. 3c confirms that the as-prepared AuNTs were single crystalline⁴⁹. More detailed information was provided by the aberration-corrected high-angle annular dark-field scanning TEM (AC-HAADF-STEM) images showing the precise surface structures of AuNTs. As shown in Fig. 3d, the edges of the AuNTs were mainly enclosed by the basal (111) planes and the stepped (211) facets, revealing the surface steps on AuNTs, which could thereby create catalytically active sites due to their under-coordinated chemical states.

Gold nanodisks (AuNDs) capped by CTAC were synthesized via tip-selective oxidative etching of AuNTs with HAuCl₄, yielding uniform circular disks with consistent (111) facets (Supplementary Fig. 8)⁵². Besides, Au obtuse-angle nanoparticles (AuNPs) were synthesized using a seed-mediated method in aqueous hexadecyltrimethylammonium bromide (CTAB) solution⁵³. The AuNPs exhibited the plasmon resonance peak of 534 nm with narrow full width at half maximum (Supplementary Fig. 9). TEM imaging (Supplementary Fig. 10) shows that their sizes and shapes are relatively uniform, with an average edge length of 35.98 ± 5.45 nm. In addition, Au nanoparticles in commercial gold carbons (Au commercial particles, AuCPs) exhibit a similar near-spherical morphology with a diameter distribution of 8.48 ± 3.00 nm (Supplementary Figs. 11 and 12). As expected, XRD

(Supplementary Figs. 13 and 14), X-ray absorption near-edge structure spectroscopy (XANES, Supplementary Fig. 15) and X-ray photoemission spectroscopy (XPS, Supplementary Fig. 16) studies suggested that all four samples (i.e., AuNTs, AuNDs, AuNPs, and AuCPs) comprised the same pure Au⁰ phase.

CO₂ electroreduction in metal-cation-free acidic media

To validate the predicted enhancement of CO₂R by EEF, we evaluated the catalytic behavior of Au-catalysts (i.e., AuNTs, AuNDs, AuNPs, and AuCPs) in acidic conditions (CO₂-saturated 0.07 M H₂SO₄, pH = 1.0, Supplementary Fig. 17 and Supplementary Table 1). A flow cell with gas diffusion electrodes (GDE) was used to promote the mass transfer of reactants (Supplementary Figs. 18 and 19), increase the local concentration of CO₂. The GDE was made by applying the catalyst ink on the carbon-based gas-diffusion layer (GDL) substrate by vacuum filtration. In typical CO₂R tests, high-purity (99.999%) pre-humidified CO₂ gas was delivered to the cathode with a constant flow rate of 20 standard cubic centimeters per minute (sccm). The liquid products were analyzed by ¹H nuclear magnetic resonance (NMR) and the gas products were measured by online gas chromatography (GC).

Product analysis with NMR showed that no liquid-phase products could be detected from the electrolysis reactions in electrolytes (Supplementary Fig. 20). Quantitative experiments (Fig. 4a) demonstrated that AuNTs exhibited a high effective current density (j_{CO}) of 122 mA cm⁻² at -1.0 V vs. RHE, exceeding 3.1, 4.1, and 8.3 times that of AuNDs (39.4 mA cm⁻²), AuNPs (29.6 mA cm⁻²), and AuCPs (14.6 mA cm⁻²), respectively. As shown in Fig. 4b, c, AuNTs exhibited higher FE_{CO} and half-cell cathodic energy efficiency (CEE, see “Materials and Methods”) in a wide range of applied potentials (-0.7 to -1.1 V

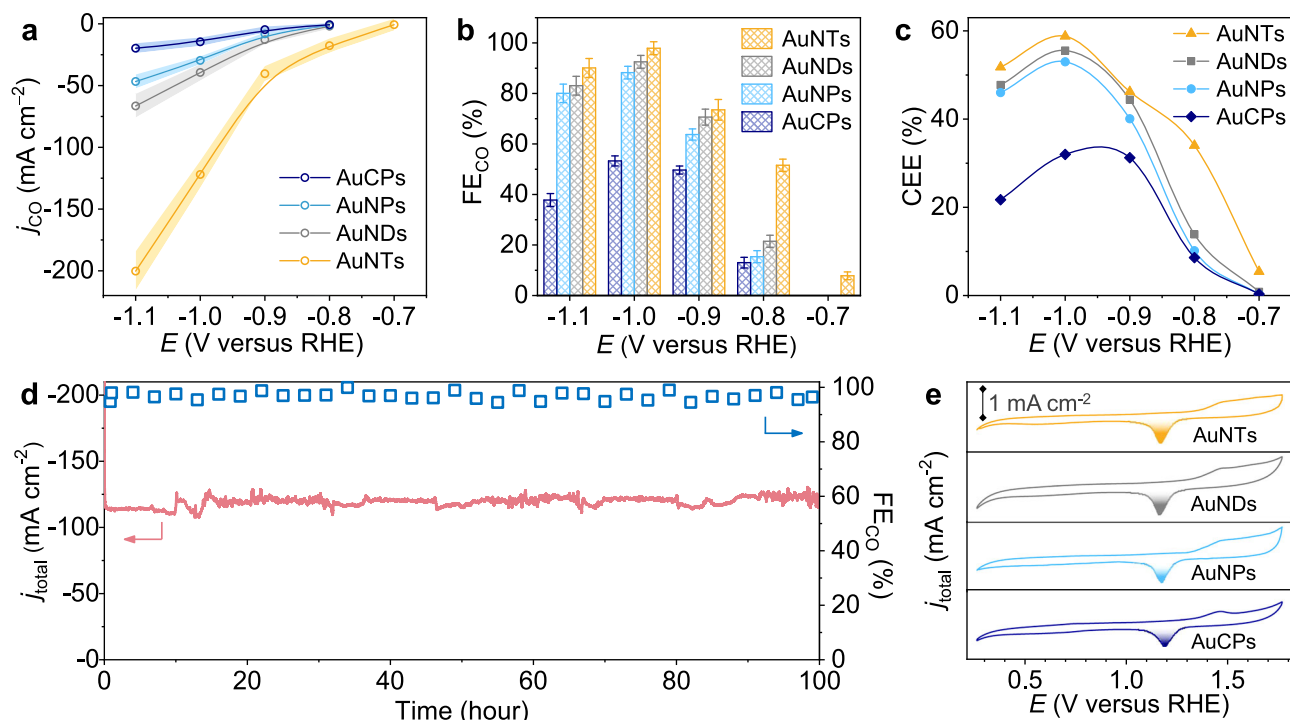


Fig. 4 | Catalytic performance of Au-catalysts for CO_2R . **a** Current density (j_{CO}) versus applied potential (E vs. RHE) for Au nanocatalysts: nanotriangles (AuNTs), nanodisks (AuNDs), nanoparticles (AuNPs), and commercial powders (AuCPs). **b** Faradaic efficiency for CO (FE_{CO}) at different applied potentials. **c** Half-cell cathodic energy efficiency (CEE) as a function of applied potential. **d** Stability test

for AuNTs at -1.0 V vs. RHE over 100 h. The total current density (j_{total}) remains stable, and FE_{CO} is consistently high, indicating durable long-term performance. **e** Cyclic voltammograms for AuNTs, AuNDs, AuNPs, and AuCPs in 50 mM H_2SO_4 . The error bars and bands correspond to the standard deviation of three independent measurements.

vs. RHE). At the applied potential of -1.0 V vs. RHE, AuNTs could exhibit a near-unity FE_{CO} with a CEE of about 59% (Fig. 4b, c). Notably, the AuNTs exhibited a stable total current density of -120 mA cm^{-2} with an average FE_{CO} of $\sim 97\%$ at -1.0 V vs. RHE during the long-term (100 h) electrolysis (Fig. 4d). Moreover, the j_{CO} could be further elevated to nearly 200 mA cm^{-2} at -1.1 V vs. RHE with an FE of $\sim 90\%$ and an EE of $\sim 52\%$ (Fig. 4a–c), providing the opportunity to promote CO production by simply applying more negative cathodic potentials while maintaining high selectivity.

In short, the AuNTs exhibit high activity, selectivity, durability, and energy efficiency for CO evolution in metal cation-free acidic solutions, representing one of the most efficient CO_2R electrocatalysts with high overall energy efficiency and CO_2 utilization (Supplementary Table 2).

Morphology effect

To elucidate the intrinsic effects of nanostructure morphology on CO_2R in metal-cation-free acidic media, we systematically compared the catalytic performance of spherical AuCPs and two-dimensional circular AuNDs. These nanostructures exhibit distinct dimensionality while maintaining similar curvature, allowing us to isolate the influence of dimensionality on CO_2R activity. Electrochemical measurements reveal that AuNDs, as two-dimensional nanostructures, exhibit significantly enhanced catalytic performance compared to spherical AuCPs. The j_{CO} of AuNDs is approximately 2.7 times higher than that of AuCPs at -1.0 V vs. RHE (Fig. 4a). This enhancement can be attributed to the increased electrochemically active surface area (ECSA, Fig. 4e and Supplementary Table 3), which provides a greater density of catalytically active sites for CO_2 adsorption and activation.

To further isolate the role of morphology from potential contributing factors of surfactant, we removed the cationic surfactant CTAC from AuNDs to obtain bare AuNDs (Supplementary Fig. 21). The

bare AuNDs exhibited higher j_{CO} than AuCPs, confirming that the 2D structure contributes to increased CO_2 reduction activity due to enhanced surface accessibility and active site exposure (Supplementary Fig. 22). However, their Faradaic efficiency (FE_{CO}) remained comparable to that of AuCPs, suggesting that the 2D morphology alone does not significantly improve catalytic selectivity in the absence of a cationic surfactant. This highlights the critical role of the cationic CTAC layer in modulating selectivity.

Despite their structural similarity to AuNTs in lateral dimensions, AuNDs exhibit significantly lower catalytic activity than AuNTs across all tested potentials (Fig. 4a). The j_{CO} of AuNDs is ~ 3.1 times lower than that of AuNTs at -1.0 V vs. RHE, which indicates that morphological effects alone cannot fully account for the enhanced catalytic performance observed in AuNTs. Given that both AuNDs and AuNTs share a two-dimensional framework, the additional enhancement observed in AuNTs suggests the presence of another key factor beyond general morphological contributions.

This comparative analysis establishes that while 2D nanostructures enhance CO_2R activity through increased surface area and active site density, the enhanced catalytic performance of AuNTs cannot be solely attributed to morphology. Instead, the presence of high-curvature tip geometries in AuNTs likely plays a crucial role by inducing strong local electric fields, which will be further explored in the next section.

Tip-enhanced electric field effects

Given that both AuNTs and AuNDs exhibit similar two-dimensional structures, lateral dimensions, and ECSA, we hypothesize that the high-curvature tips of AuNTs induce strong local electric fields, thereby facilitating CO_2 activation and enhancing reactivity.

To experimentally probe this hypothesis, we performed in-situ attenuated total reflection surface-enhanced infrared absorption

spectroscopy (ATR-SEIRAS) to analyze CO₂ adsorption and activation dynamics on AuNTs at varying potentials (Supplementary Fig. 23). The intensification of adsorbed CO peaks suggests an increase in the quantity of adsorbed intermediates. To further elucidate the tip effect on the local electric field, we analyzed the Stark tuning shifts of adsorbed CO species on AuNTs under varying potentials. The Stark shift, which reflects the interaction between the localized electric field and the dipole moment of adsorbed species, is significantly larger for AuNTs compared to AuNDs (Supplementary Fig. 24). This pronounced shift provides quantitatively direct spectroscopic evidence that the sharp tips of AuNTs generate a stronger localized electric field. Kelvin probe force microscopy (KPFM) measurements further corroborate this localized electric field enhancement. Surface potential mapping reveals a pronounced increase in potential at the sharp tips of AuNTs, whereas AuNDs exhibit a more uniform potential distribution (Supplementary Fig. 25). This tip-induced potential contrast provides direct experimental evidence of enhanced charge accumulation at the apexes of AuNTs, in agreement with finite element simulations (Fig. 2d).

To isolate the effect of tip-enhanced electric fields from morphological contributions, we synthesized passivated AuNTs, in which the sharp tips were selectively rounded to suppress local electric field effects while maintaining the overall triangular morphology (Supplementary Fig. 26). Electrochemical testing revealed that compared to AuNTs, passivated AuNTs exhibited a substantial reduction in j_{CO} and FE_{CO} (Supplementary Fig. 27), closely resembling the performance of AuNDs (Fig. 4a–c). Given that both passivated AuNTs and AuNDs share similar 2D structures, this result confirms that the higher performance of AuNTs originates from their sharp tips rather than their basal two-dimensional framework alone.

Taken together, these experimental and computational results conclusively demonstrate that the enhanced catalytic performance of AuNTs arises from the synergy between their 2D morphology and tip-enhanced local electric fields. The sharp tips of AuNTs concentrate charge, amplify local electric fields, and facilitate CO₂ activation, which in turn accelerates reaction kinetics. This understanding forms the basis for the next section, where we analyze the synergistic effects of morphology and electric field enhancement in achieving optimal CO₂R performance.

Synergistic effects of nanostructure and local electric field

Tafel analysis elucidated the accelerated kinetics for CO evolution on AuNTs. Previous studies suggest that during two-electron CO₂R, the first one-electron step of CO₂ to COOH* or CO₂⁻ intermediates determines the rate for the combined process³⁸ and hence the Tafel slope⁵⁴. As shown in Supplementary Fig. 28, the Tafel slope measured for the AuNDs, AuNPs and AuCPs of 117, 121, and 123 mV dec⁻¹ agrees well with prior reports⁵⁵, whereas the much lower Tafel slope of 43 mV dec⁻¹ obtained for the AuNTs indicates a faster first-electron transfer step^{38,55} and confirms the intrinsic advantage of AuNTs in CO₂ reduction^{56,57}. Electrochemical impedance spectroscopy (EIS) measurements also corroborated that AuNTs exhibit the smallest semi-circle diameter of the Nyquist plot, reflecting an acceleration of the charge transfer process at electrode/solution interfaces (Supplementary Fig. 29).

Intrinsic performances can be further compared by normalizing j_{CO} to the ECSA. The AuNTs still exhibited the highest ECSA-normalized j_{CO} at -1.0 V vs. RHE (2.21 mA cm⁻²), significantly surpassing AuNDs (0.81 mA cm⁻²), AuNPs (0.54 mA cm⁻²), and AuCPs (0.30 mA cm⁻²) (Supplementary Fig. 30), indicating higher intrinsic CO₂R activities due to the existence of the tip-enhanced electric field. This finding confirms that the enhanced catalytic activity of AuNTs is not solely attributed to their larger surface area but is an inherent result of tip-enhanced local electric fields, which facilitate CO₂ adsorption and electron transfer. Therefore, by combining an increased number of

active sites with higher average intrinsic activity per site, AuNTs achieve the highest overall CO₂R performance among the four catalysts.

These results demonstrate that the enhanced CO₂R activity of AuNTs is primarily governed by the synergy between their 2D morphology and tip-enhanced local electric fields. The 2D morphology increases the density of electrochemically active sites, while the sharp tips generate localized electric fields that polarize CO₂ molecules, reduce activation barriers, and facilitate electron transfer. While these structural features play a decisive role in improving catalytic activity, additional factors may further influence CO₂R selectivity. In particular, the biomimetic proton rejection mechanism induced by the cationic surfactant layer will be discussed in the next section.

Improving CO₂R selectivity by bionic design

Generally, where water can pass, (hydrated) protons can traverse. However, aquaporin, a specialized protein channel in the cell membrane, selectively permits the passage of electrically neutral water molecules while effectively repelling positively charged protons. This selective function is attributed to the positively charged guanidinium group on an arginine residue located near a constricting histidine within the channel (Fig. 1b). Previous reports have shown that the addition of quaternary ammonium salts to the electrolyte can be expected to act as alkali metal ions^{58–62}. In our system, the cationic surfactant layer of CTAC on the Au surface mimics the function of aquaporin. This layer carries positive charges, enabling the selective passage of electrically neutral CO₂ molecules while obstructing proton transport. Moreover, beyond electrostatic proton exclusion, such positively charged quaternary ammonium groups (CTA⁺) may also contribute to a second-sphere electrostatic environment that influences CO₂ activation, conceptually analogous to the “electrostatic stabilization” mechanism proposed for ammonium-functionalized molecular catalysts⁶³. While we do not claim direct stabilization of reaction intermediates here, this conceptual framework provides a plausible context for interpreting the improved CO₂R selectivity observed for cationic surfactant-modified catalysts discussed below. It should be emphasized that this analogy operates at the molecular-functional level rather than structural mimicry—the CTAC bilayer reproduces the electrostatic principle of proton exclusion found in aquaporins, rather than imitating their channel architecture. In addition, the interdigitated alkyl chains within the CTAC layer create a hydrophobic interfacial region of reduced water activity and hydrogen-bond density, analogous to the hydrophobic confinement discussed in recent reports^{64,65}. This hydrophobic microenvironment complements the electrostatic proton-blocking effect, collectively stabilizing the local reaction interface and improving CO₂R selectivity under strongly acidic conditions.

The FE_{CO} of AuNTs, AuNDs, and AuNPs, each capped with hexadecyltrimethylammonium halide surfactants, significantly surpasses that of surfactant-free AuCPs (Fig. 4b). This suggests that the CTAC surfactant on the AuNTs catalyst (Supplementary Fig. 31) may function analogously to aquaporin in electrolytes. The adsorption behavior of CTAC on AuNTs during electrocatalytic reactions was analyzed using in-situ ATR-SEIRAS spectroscopy. The results reveal that, under constant potential (-0.7, -1.0, -1.1 V vs. RHE), CTAC remains stably adsorbed on the gold surface, as indicated by the no obviously changed ν_{CH} peak intensities at 2864 and 2960 cm⁻¹ in the in-situ ATR-SEIRAS spectra (Fig. 5a and Supplementary Fig. 32). Furthermore, variable potential experiments further explored CTAC adsorption behavior under different applied voltages (Supplementary Fig. 23). Upon applying a positive voltage, the upward peaks at 2860 and 2960 cm⁻¹ reflected a decrease in CTAC coverage relative to the open circuit potential. Conversely, as the voltage became increasingly negative, these peaks inverted and intensified, indicating progressive CTAC adsorption. These observations demonstrate that CTAC

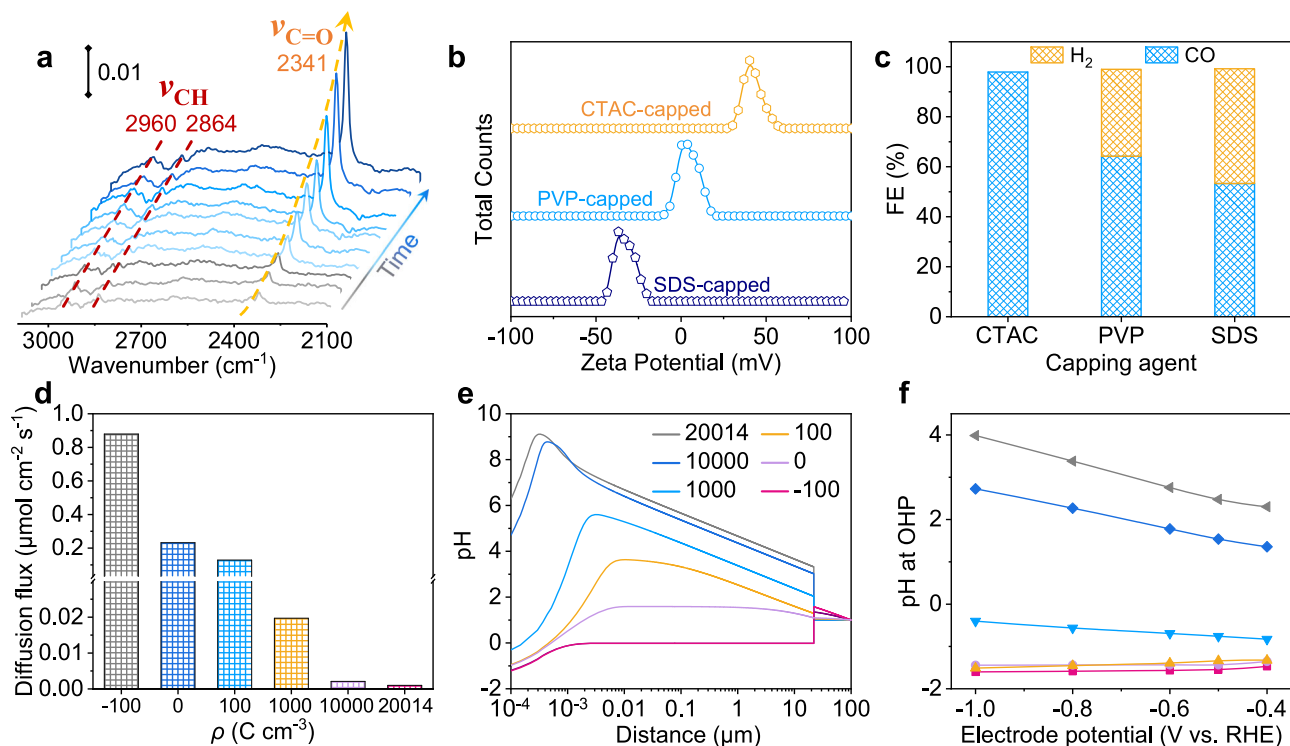


Fig. 5 | Influence of surfactant capping and charge on CO₂R. **a** In-situ ATR-SEIRAS spectra illustrating the adsorption behavior of CTAC and CO₂ on AuNTs during electrocatalytic reactions at -1.0 V vs. RHE. **b** Zeta potential distributions for AuNTs capped with CTAC, PVP, and SDS. CTAC-capped AuNTs exhibit positive zeta potential, PVP-capped AuNTs show neutral potential, and SDS-capped AuNTs display negative potential. **c** FE_{CO} for AuNTs capped with different surfactants. **d** Migration rate of H⁺ as a function of charge density within the surfactant layer, measured at an electrode potential of -1.0 V vs. RHE, at $15\ \mu\text{m}$ outside surfactant

layer. The cationic surfactant layer significantly reduces the migration rate of H⁺. **e** pH profiles near the cathode at -1.0 V vs. RHE for different surfactant charges. A positively charged surfactant layer leads to a higher pH near the electrode surface. **f** Local pH at the outer Helmholtz plane (OHP) for different potentials on AuNTs catalysts covered by surfactant layers with different charge density (unit: C·cm⁻³) in H₂SO₄ (pH 1.0). The presence of a positively charged surfactant layer increases the local pH at the OHP.

primarily exists as CTA⁺ on the Au surface, with its adsorption behavior influenced by the applied voltage. Background spectra, collected before and after the in-situ ATR-SEIRAS measurements under both constant and variable potentials (Supplementary Fig. 33), showed no significant changes, further confirming that CTAC remains stably adsorbed on the Au surface throughout the electrocatalytic process.

To understand the effect of the cationic surfactant on CO₂ reduction in acidic electrolytes devoid of alkali cation, we performed experiments using the following control samples (Supplementary Fig. 21): CTAC-capped AuNTs and bare AuNTs (CTAC removed), CTAC-capped AuNDs and bare AuNDs (CTAC removed). The CTAC-capped AuNTs achieved a FE_{CO} of $\sim 100\%$, while bare AuNTs showed a reduced FE_{CO} of 61.9% (Supplementary Fig. 34). The CTAC-capped AuNDs achieved a FE_{CO} of 92.5%, while bare AuNDs showed a much lower FE_{CO} of 54.3%. These results demonstrate that the CTAC capping layer plays a crucial role in enhancing the CO₂ reduction selectivity by suppressing competing HER, particularly in acidic conditions. Without the CTAC layer, the FE_{CO} drops significantly, even for AuNTs, which inherently possess a high-curvature structure that promotes CO₂ activation.

In addition, we conducted experiments with AuNTs capped with different surfactants—cationic surfactant CTAC, nonionic surfactant polyvinyl pyrrolidone (PVP), and anionic surfactant sodium dodecyl sulfate (SDS)—and simulated the process with molecular dynamics (MD) and Poisson-Nernst-Planck (PNP) modelings. The zeta potential measurements revealed that CTAC-capped, PVP-capped, and SDS-capped AuNTs exhibited positive, neutral, and negative charges, respectively (Fig. 5b). Correspondingly, the FE_{CO} values were nearly 100%, 62.2%, and 53.3% (Fig. 5c). The MD simulations (Supplementary Data 2) on three surface models of Au/CTAC, Au/PVP, and Au/SDS

reveal the CTAC-capped surface exhibits the strongest proton-repelling ability (CTAC > PVP > SDS), which provides an effective shield to proton transport and reduces proton availability near the surface (Supplementary Fig. 35). These results suggest that cationic surfactants can inhibit the HER, due to electrostatic repulsion between the positively charged surfactant and protons. In contrast, nonionic surfactants exhibit minimal impact on proton behavior, while anionic surfactants could promote HER, through electrostatic attraction of protons. This indicates that the charge characteristics of surfactants are pivotal in modulating FE_{CO} of CO₂R.

Finite element method simulations based on a Poisson-Nernst-Planck model⁶⁶ were subsequently performed to elucidate the role of the cationic surfactant layer in inhibiting H⁺ mass transport (Supplementary Fig. 36). The Stern layer, located between the cathode and the outer Helmholtz plane (OHP), is devoid of charged species. A surfactant layer with varying charge properties, positioned outside the OHP, exhibited a charge density of immobilized ionic sites (ρ) that was determined to be $+20014\ \text{C}\cdot\text{cm}^{-3}$, as detailed in the “Materials and Methods” section (Supplementary Figs. 37 and 38). According to the experimental loading of CTAC-capped AuNTs on the electrode, the thickness of the surfactant layer was set to $22.1\ \mu\text{m}$ in the simulation (Supplementary Figs. 36 and 38). Beyond this surfactant layer, the simulation environment included movable H⁺, OH⁻, and SO₄²⁻ ions. The efficiency of H⁺ reduction is constrained by the mass transport of H⁺. At -1.0 V vs. RHE, the migration rate of H⁺ outside the surfactant layer decreases as ρ increases, indicating that the cationic surfactant layer can screen the electric field and thereby reduce the migration rate of H⁺, while the anionic surfactant layer exerts the opposite effect (Fig. 5d).

The charge of the surfactant layer also affects the local pH near the cathode. Figure 5e and Supplementary Fig. 39 present the pH profiles and proton concentration at -1.0 V vs. RHE in a pH 1.0 electrolyte, comparing different charge properties of the surfactant layer. When the surfactant layer is uncharged, the pH within the region 2 nm to 22.1 μm from the OHP is higher than the bulk pH due to concentration polarization. However, within 2 nm vicinity of the OHP, the pH is lower than the bulk pH, as protons are electrostatically attracted to the cathode. Figure 5f further illustrates the pH at the OHP under varying electrode potentials. When the surfactant is either neutral or negatively charged, a negative shift in the electrode potential does not substantially increase the pH at the OHP. In contrast, with a surfactant layer carrying positive charge density greater than $+1000\text{ C}\cdot\text{cm}^{-3}$, the pH within the surfactant layer rises sharply (Fig. 5e and Supplementary Fig. 39), and the local pH at the OHP increases as the electrode potential shifts negatively beyond -0.4 V vs. RHE (Fig. 5f). Notably, when the charge density exceeds $+10000\text{ C}\cdot\text{cm}^{-3}$, the pH at the OHP surpasses the bulk pH at the potential region below -0.4 V vs. RHE. Therefore, a local pH increases at the OHP driven by H^+ reduction is observed only when the cathode is capped by a cationic surfactant layer. During CO_2 reduction, OH^- anions generated from CO_2 reduction process can neutralize H^+ and further elevate local pH^{10} . Therefore, the local pH under the CO_2 reduction condition is expected to be higher than the value shown in Fig. 5f.

These findings highlight the crucial role of the surfactant layer in modulating the local concentration of H^+ , thereby impacting the kinetics of hydrogen evolution in acidic electrolytes. Specifically, the presence of a cationic surfactant layer can effectively impede H^+ transport through Donnan exclusion, with this inhibition becoming progressively pronounced as the positive charge density intensifies, leading to a concomitant decrease in the diffusion rate of H^+ .

Discussion

In summary, we demonstrated that the polarization and repulsion effects observed in CTAC-capped AuNTs with sharp-tip structures significantly enhance CO_2 reduction while concurrently suppressing the HER in metal-cation-free acidic electrolytes. The high-intensity local electric fields generated at the AuNTs tips disrupt the nonpolar state of CO_2 molecules, inducing dipole moments by shifting and deforming the electron cloud. This increased polarizability of CO_2 facilitates its adsorption, making the process thermodynamically spontaneous, weakening the $\text{C}=\text{O}$ bond, and lowering the energy barrier of the RDS, thereby improving CO_2 reduction activity. Simultaneously, the quaternary ammonium surfactant's cationic sites impede H^+ migration, effectively inhibiting the HER in acidic media. This synergistic strategy marks a substantial advancement in CO_2 reduction technology and holds significant potential for broader applications in electrocatalysis and clean energy conversion.

Methods

Materials

Hexadecyltrimethylammonium chloride (CTAC, 25 wt% in water), gold(III) chloride trihydrate ($\text{HAuCl}_4\cdot 3\text{H}_2\text{O}$, $\geq 49.0\%$ Au basis), polyvinylpyrrolidone (PVP, average molecular weight: 10 000), L-ascorbic acid (AA assay: 99.7–100.5%), potassium iodide (KI, $\geq 99.5\%$), sodium iodide (NaI, $\geq 99.5\%$), sodium borohydride (NaBH_4 , 99%), sodium hydroxide (NaOH, $\geq 99\%$), ethanol ($> 99.9\%$, absolute grade), sulfuric acid (H_2SO_4 , 96%), nitric acid (HNO_3 , 69%), and hydrochloric acid (HCl, 36%) were purchased from Sigma-Aldrich. Carbon black (Vulcan XC-72) was obtained from Carbot Co. (USA). Nafion PFSA polymer dispersions (D520, 5% w/w in water, 1-propanol, and ethanol) were purchased from DuPont (USA). The carbon-based gas-diffusion layer (GDL) substrate was purchased from Freudenberg (Germany). All chemicals were used as received without further treatment. Ultrapure water (resistivity 18.2 $\text{M}\Omega\text{ cm}$ at 25 $^\circ\text{C}$) obtained by the Milli-Q system

was used in all experiments. All glassware was cleaned with aqua regia ($V_{\text{HCl}}: V_{\text{HNO}_3} = 3:1$), thoroughly rinsed with copious amounts of ultrapure water, and subsequently boiled at least five times in ultrapure water.

Synthesis of the AuNTs capped by CTAC

A CTAC-mediated reduction protocol was employed to prepare AuNTs^{49,50}. In a typical synthesis, an aqueous CTAC solution (0.1 M, 1.6 mL) was diluted with 8 mL of ultrapure water, followed by addition of KI (0.01 M, 75 μL). Sequential introduction of equimolar HAuCl_4 (25.4 mM, 80 μL) and NaOH (0.1 M, 20.3 μL) generated a pale-yellow mixture. Upon injection of ascorbic acid (0.064 M, 80 μL) under moderate stirring (~ 700 rpm), the solution gradually became colorless, indicative of the Au(III) to Au(I) reduction. Subsequent injection of NaOH (0.1 M, 10 μL) with rapid shaking triggered nucleation and anisotropic growth, yielding a blue colloidal dispersion.

Purification of the AuNTs capped by CTAC

The crude AuNT dispersion was purified using a CTAC-induced flocculation method adapted from Scarabelli et al.^{50,67}. A concentrated CTAC stock (0.2 M) was added to the as-synthesized solution to promote selective aggregation of nanotriangles via depletion interactions. After standing overnight, the supernatant was discarded, and the precipitate was redispersed in 500 μL of 40 mM CTAC. The gold content ($\approx 17.5\text{ mM Au}^0$) was estimated from the 400 nm absorbance following standard calibration procedures^{68,69}.

Synthesis of AuNDs

AuNDs were derived from controlled oxidative reshaping of pre-formed AuNTs following a modified Mirkin-type protocol⁵². Briefly, HAuCl_4 (10 mM) was mixed with an AuNT–CTAC dispersion (23 pM AuNTs, 50 mM CTAC) to reach 8 μM HAuCl_4 . The reaction was maintained at 28 $^\circ\text{C}$ for 4 h, after which the mixture was centrifuged (9400 rcf, 10 min) to remove Au(I) species and redispersed in 50 mM CTAC to prevent secondary deposition.

Synthesis of AuNPs

AuNPs were synthesized through a classical seed-mediated growth route⁵³. In brief, small Au seeds were generated by quickly injecting an ice-cold, freshly prepared NaBH_4 solution (0.01 M, 0.3 mL) into an aqueous mixture containing HAuCl_4 (0.01 M, 0.125 mL) and CTAB (0.1 M, 3.75 mL) under vigorous inversion. The reaction mixture was aged for 1 h at room temperature to ensure complete reduction of Au(III) and stabilization of the seeds. For particle growth, a separate solution was prepared by sequential dissolving CTAB (0.1 M, 6.4 mL), HAuCl_4 (0.01 M, 0.8 mL), and ascorbic acid (0.1 M, 3.8 mL) in 32 mL of deionized water. The aged seed suspension was diluted tenfold with water and then added all at once to the growth solution, followed by gentle inversion for approximately 10 s. The dispersion was then kept undisturbed overnight, yielding well-defined AuNPs.

PVP or SDS coating of AuNTs

For polymer or surfactant exchange⁵⁰, AuNTs@CTAC were centrifuged (1800 $\times g$, 15 min, 30 $^\circ\text{C}$), the supernatant removed, and the pellet redispersed in 0.1 M CTAC (50 μL). After brief sonication and dilution to 0.5 mM Au^0 , a 10 g L^{-1} PVP or SDS solution (prepared by 10 min sonication) was added under vigorous stirring to reach a final PVP or SDS concentration of 1 g L^{-1} . The mixture was stirred overnight at ambient temperature to complete ligand exchange.

CTAC removal of AuNTs and AuNDs

The CTAC removal process was carried out as follows: First, 5 mg of carbon black was dispersed into a mixture of 965 μL of catalyst dispersion (3.45 g L^{-1} in water) and 3 mL of ethanol. The resulting solution was sonicated for 40 min to ensure uniform dispersion. Subsequently, the solution was dissolved in 100 mL of a hydrochloric acid-ethanol

solution (HCl:ethanol = 1:9, v/v) and refluxed at 78 °C for 12 h. After refluxing, the product was collected via centrifugation, followed by alternating washing with ethanol and deionized water to remove the CTAC. The washing process was repeated several times to ensure the complete removal of the surfactant. The final catalyst was dried under a vacuum at 50 °C to obtain the CTAC-free (bare) AuNTs and AuNDs catalyst.

Electrode preparation

Catalyst (AuNTs, AuNDs, and AuNPs) inks were prepared by dispersing 5 mg of carbon black in the mixture of 80 μL of Nafion, 965 μL of catalyst dispersions (3.45 g L^{-1} in water), and 3 mL of isopropanol under sonication for 40 min. Catalyst (AuCPs) inks were prepared by dispersing 8.33 mg of AuCPs (40% gold supported on Vulcan XC-72) in the mixture of 80 μL of Nafion, 965 μL of water, and 3 mL of isopropanol under sonication for 40 min. The GDE was made by seriatim spraying about 2.43 mL of the catalyst ink on the carbon-based gas-diffusion layer (GDL) substrate with an effective electrode geometric area of $2 \times 1 \text{ cm}^2$ and a metal loading of about 1.0 mg cm^{-2} .

Electrocatalytic CO₂R tests in the flow cell

The CO₂R was performed in a three-electrode flow cell, which was composed of a catalyst-deposited GDE as the working electrode, an Ag/AgCl reference electrode, and a platinum plate anode. The cathodic and anodic compartments were separated by a Nafion 115 proton exchange membrane. The membrane was pretreated in 5% H₂O₂ solution (80 °C, 1 h), soaked in 0.5 M H₂SO₄ solution (80 °C, 1 h), immersed in ultrapure water (80 °C, 1 h), and then washed with ultrapure water several times before use. A high-purity (99.999%) pre-humidified CO₂ gas flow with a constant flow rate of 20 sccm monitored by a mass flow controller was delivered behind the GDE to diffuse into the catalyst layer presented at the catalytic area ($2 \times 1 \text{ cm}^2$). The 0.07 M H₂SO₄ (pH = 1.0, Supplementary Fig. 17) solution²⁴ was employed as the electrolyte and circulated (5 mL min⁻¹, 30 mL each for the catholyte and anolyte) through the electrochemical cell with a peristaltic pump. The reactions were run for 1 h before the products were collected for analysis. The outlet gas flow, which passed directly through gas chromatography, was measured by a portable electronic flow meter (Restek ProFLOW 6000) to evaluate the FE_{CO} accurately. An online gas chromatograph (GC, Shimadzu GC-2014C) equipped with a packed column (MS-13X), a thermal conductivity detector (TCD), and a flame ionization detector (FID) was used to quantify the gaseous products. And the possible liquid products were analyzed by ¹H nuclear magnetic resonance (NMR). Typically, 500 μL of electrolyte was extracted from the cathodic chamber after electrolysis and was mixed with 100 μL of D₂O. Then, 0.05 μL of dimethyl sulfoxide (DMSO) was added as an internal standard. The one-dimensional ¹H spectrum was measured with water suppression using a solvent pre-saturation technique.

In-situ ATR-SEIRAS measurements

Attenuated total-reflection surface-enhanced infrared absorption spectroscopy (ATR-SEIRAS) was employed to monitor the reaction intermediates under electrochemical CO₂ reduction conditions. Measurements were carried out on a Thermo Nicolet 8700 spectrometer equipped with a liquid-nitrogen-cooled mercury-cadmium-telluride (MCT) detector. A gold film (~60 nm thick) was chemically deposited on a silicon prism via a two-step wet-chemical procedure. Prior to Au deposition, the reflective surface of the Si prism was mechanically polished with diamond suspension, sonicated in deionized water, and treated in piranha solution (H₂SO₄: H₂O₂ = 7: 3 v/v) for 2 h to remove organic residues.

After film preparation, ~30 μL of catalyst ink was drop-cast onto the Au-coated surface and dried in air. The modified prism was then assembled into a custom spectroelectrochemical cell, serving as the

working electrode. A Pt mesh (1 \times 1 cm) and an Ag/AgCl electrode positioned through a Luggin capillary were used as counter and reference electrodes, respectively. Prior to data collection, CO₂ gas was bubbled through the cell for 30 min to replace the atmosphere, followed by a 20 min equilibration to ensure complete dissolution.

Spectra were recorded under potentiostatic or potential-step conditions using a CHI electrochemical workstation. The differential spectra were processed as $\Delta R/R = (E_S - E_R)/E_R$, where E_S and E_R represent sample and reference spectra, respectively. Unless otherwise noted, the spectral resolution was 4 cm^{-1} .

Characterizations

Powder X-ray diffraction (PXRD) patterns were acquired on a Rigaku MiniFlex 600 diffractometer with Cu K α radiation ($\lambda = 0.154056 \text{ nm}$) operated at 40 kV and 50 mA, with a scan rate of 1° min⁻¹. UV-vis absorption spectra were collected on a Shimadzu UV-2600 spectrophotometer (slit width = 2.0 nm; resolution = 0.5 nm). ¹H NMR spectra were recorded on a Bruker Ascend 400 MHz spectrometer using D₂O as solvent; chemical shifts are referenced to the residual solvent signal or TMS (0.00 ppm). Elemental compositions were quantified by inductively coupled plasma optical emission spectroscopy (ICP-OES, Agilent 720) under the following conditions: RF power 1.2 kW, plasma gas flow 15.0 L min⁻¹, auxiliary gas flow 1.5 L min⁻¹, nebulizer gas flow 0.75 L min⁻¹, injection delay 15 s, stabilization delay 15 s. X-ray photoelectron spectroscopy (XPS) was carried out on a Thermo Scientific ESCALAB 250 Xi system equipped with a monochromatic Al K α source ($h\nu = 1486.6 \text{ eV}$). Spectra were calibrated against the C 1s peak at 284.8 eV, and measurements were performed at a base pressure of $\approx 1 \times 10^{-9}$ mbar (analysis area $\approx 500 \mu\text{m}$, sampling depth $\approx 10 \text{ nm}$). Au L-edge X-ray absorption fine structure (XAFS) spectra were collected at beamline BL01C1 of the National Synchrotron Radiation Research Center (NSRRC) in fluorescence mode using a solid-state detector. Gold foil was used as the reference standard. Data reduction and fitting were performed with the Athena and Artemis codes. For the X-ray absorption near-edge structure (XANES) region, $\mu(E)$ was background-subtracted and normalized, and the results are presented as normalized absorption for all samples and standards. Transmission electron microscopy (TEM) was performed on JEOL JEM-2100 (200 kV) and FEI Tecnai G2 F30 (300 kV) microscopes. High-angle annular dark-field scanning transmission electron microscopy (HAADF-STEM) imaging and elemental mapping were acquired on the FEI Tecnai G2 F30 operated at 300 kV, while atomic-resolution HAADF-STEM measurements were carried out using an FEI Themis Z with double aberration correctors.

Measurements of Au and CTAC ratio using XPS analysis

We conducted XPS analysis to determine the content of gold (Au) and cetyltrimethylammonium chloride (CTAC) on the surface of AuNTs. The following steps were taken: First, integration of peak areas: The areas under the identified peaks were integrated. The peak areas obtained were: Au 4f: -7805, N 1s: -132380. Second, sensitivity factor correction: The peak areas were corrected using the relative sensitivity factors (RSF) for Au 4f and N 1s, which are 9.58 and 1.8, respectively. The corrected peak areas were: Corrected Au 4f area: -814.72, Corrected N 1s area: -73544.44. Last, atomic ratio calculation: The atomic ratio of N to Au was calculated as follows:

$$\text{Atomic ratio} = \frac{\text{Corrected N 1s area}}{\text{Corrected Au 4f area}} = \frac{\frac{\text{N 1s area}}{\text{N 1s RSF}}}{\frac{\text{Au 4f area}}{\text{Au 4f RSF}}} \quad (1)$$

The high atomic ratio of N to Au is 90.27, indicating a significant presence of CTAC on the surface of the AuNTs.

Determination of charge density of charge layer

To quantify the number of Au atoms on the electrode, we begin by determining the molar amount of Au using the relation:

$$\text{Number of Au atoms} = n_{\text{Au}} \times N_A = \frac{m_{\text{Au}}}{M_{\text{Au}}} \times N_A \quad (2)$$

where the total amount of Au deposited on the electrode is 2 mg, the molar mass of Au is 197 g mol⁻¹, and Avogadro's number is 6.022 × 10²³ mol⁻¹. This yields a total of approximately 6.11 × 10¹⁸ Au atoms.

Next, the number of CTAC molecules on the electrode is estimated. Given an atomic ratio of Au to N of 1:90.27, the total number of nitrogen atoms is calculated as:

$$\text{Number of N atoms} = 6.11 \times 10^{18} \text{ atoms} \times 90.27 = 5.52 \times 10^{20} \text{ atoms} \quad (3)$$

Since each CTAC molecule contains one nitrogen atom, the total number of CTAC molecules is equal to the number of nitrogen atoms, resulting in 5.52 × 10²⁰ CTAC molecules.

To compute the total charge *Q*, we recognize that each CTAC molecule carries one positive charge, with an electron charge of 1.602 × 10⁻¹⁹ C. The total charge is therefore:

$$Q = 5.52 \times 10^{20} \text{ molecules} \times 1.602 \times 10^{-19} \text{ C molecule}^{-1} = 88.46 \text{ C} \quad (4)$$

The volume of the electrode surface layer *V* is determined using the surface layer thickness *d* of 22.1 micrometers and the electrode area *A* of 2 cm²:

$$V = A \times d = 2 \text{ cm}^2 \times 22.1 \times 10^{-4} \text{ cm} = 4.42 \times 10^{-3} \text{ cm}^3 \quad (5)$$

The volume charge density ρ_v is calculated as:

$$\rho_v = Q/V = 88.46 \text{ C} / 4.42 \times 10^{-3} \text{ cm}^3 = 20013.57 \text{ C cm}^{-3} \quad (6)$$

Notably, the surface charge density ρ_s can also be estimated using the electrode area:

$$\rho_s = Q/A = 88.46 \text{ C} / 2 \text{ cm}^2 = 44.23 \text{ C cm}^{-2} \quad (7)$$

Calculation of Faradaic efficiency (FE)

The FE for CO evolution was measured based on the definition of FE:

$$FE_{\text{CO}} = \frac{Q_{\text{CO}}}{Q_{\text{T}}} \times 100\% \quad (8)$$

Q_{T} and Q_{CO} can be obtained from the following equations:

$$Q_{\text{T}} = \int_0^t I(t) dt \quad (9)$$

$$Q_{\text{CO}} = 2 \times n_{\text{CO}} \times F \quad (10)$$

where n_{CO} is the molar amount of the produced carbon monoxide measured by gas chromatograph, *F* is the Faradaic constant (96484 C mol⁻¹), and *t* is the total reaction time for reducing carbon dioxide.

Calculation of partial current density of formate (j_{CO})

$$j_{\text{CO}} = j_{\text{total}} \times FE_{\text{CO}} \quad (11)$$

where j_{total} is the total current density obtained from the chronoamperometry tests.

Calculation of half-cell cathodic energy efficiency (CEE)

Half-cell cathodic energy efficiency (CEE) quantifies the ratio of the energy effectively used for CO₂ reduction to the total energy input in the electrolysis process. The calculation of half-cell CEE assumed a zero overpotential of the oxygen evolution reaction at the anode side, which is shown in the equation below⁷⁰:

$$CEE = \frac{[1.23 + (-E_{\text{CO}})] \times FE_{\text{CO}}}{1.23 + (-E_{\text{cathode}})} \quad (12)$$

where $E_{\text{CO}} = -0.109$ V is the standard thermodynamic potential of CO₂/CO (vs. RHE), FE_{CO} is the Faradaic efficiency of CO production, and E_{cathode} is the applied cathode potential vs. RHE.

ECSA measurement

The ECSA was determined via cyclic voltammetry in 50 mM H₂SO₄, utilizing the well-established hydrogen underpotential deposition method. Specifically, we integrated the charge of the hydrogen adsorption peak obtained from cyclic voltammetry scans. Cyclic voltammograms were recorded in a potential range of 0.05 to 1.45 V (versus SCE) at a scan rate of 50 mV s⁻¹ and repeated until stable traces were obtained. The ECSA was calculated using the equation:

$$ECSA = \frac{Q_{\text{H}}}{Q_{\text{ref}} \times C_{\text{Au}}} \quad (13)$$

where Q_{H} is the integrated charge of the hydrogen adsorption peak obtained from CV scans, $Q_{\text{ref}} = 448 \mu\text{C cm}^{-2}$ is the reference charge density for a monolayer of hydrogen adsorption on Au, and C_{Au} is the metal loading on the electrode.

DFT calculations for dipole moment and electrostatic potential

Quantum chemical studies are performed using DFT implemented in the GAUSSIAN 16 package⁷¹. Geometry optimization and frequency analysis are calculated at B3LYP hybrid functional⁷² with GD3BJ dispersion correlation at 6-31G(d) basis sets. The structures are also optimized under different magnitudes of the external electric field⁷³ along the X axis. The electrostatic potential surfaces (ESP) diagram and the dipole moment were performed by Multiwfn 3.8⁷⁴ and VMD v 1.9.3⁷⁵ molecular visualization software. The bonding energy of C = O is calculated as follows: $E_{\text{b}} = E(\text{C}=\text{O}) + E(\text{O}) - E(\text{CO}_2)$.

Finite element analysis

Secondary currents and species diffusion on the electrode surface were established based on COMSOL to compare the effect of different electrode shapes⁷⁶. COMSOL Multiphysics 6.2 described the species concentration migration diffusion, potential distribution, and current transport. A geometrical model was created with an electrolyte region of 200 nm in length, width, and height, an equilateral triangle with 70 nm side lengths in the region, a truncated octahedron with size of 36 nm, and a sphere with a radius of 9 nm to characterize the electrode morphology. Since the tip effect of the triangle is larger than that of the obtuse-angle and spherical particles, the electric field and current within the electrolyte converge toward the tip of the triangle, while the species diffusion is subjected to the electric field, migrates toward the bottom, and is guided by the electric field to converge in the tip region of the particles. The main boundary conditions of the model: the top loading current density is 10³ A m⁻², and the electrolyte on the upper surface maintains a 10² mol m⁻³ ion concentration to equivalently characterize the overall electrolyte. The exchange current density at the electrode surface conformed to the Butler–Volmer equation. The

secondary current can be obtained from the following equations:

$$\nabla \bullet i_l = Q_l \quad (14)$$

$$i_l = -\sigma_l \nabla \phi_l \quad (15)$$

where i_l is the electrolyte current, ϕ_l is the electrolyte potential, σ_l is the electrolyte conductivity (0.055 S m^{-1}). Due to the charged surface modifiers, ρ_s (44.23 C cm^{-2}) was introduced on the electrode surface.

The electrochemical module in COMSOL was used to obtain the CO_2 to CO reaction current density using the Butler–Volmer equation:

$$i_{loc} = i_0 \left[\exp\left(\frac{\alpha_a F \eta}{RT}\right) - \exp\left(\frac{\alpha_c F \eta}{RT}\right) \right] \quad (16)$$

where α_a and α_c are the dimensionless anodic and cathodic charge transfer coefficients, respectively, F is the Faraday constant, R is the universal gas constant, and T is temperature, taken to be 298.15 K. The exchange current density i_0 obeys the Arrhenius law:

$$i_0 \propto \exp\left(-\frac{E_a}{k_B T}\right) \quad (17)$$

where k_B is the Boltzmann constant, and E_a is the activation energy of the CO_2 to CO reaction, which was experimentally obtained to be 0.59 eV.

PNP simulation model

A one-dimensional stationary simulation was done with COMSOL Multiphysics. Nernst Planck equation and the Poisson equation were employed for the simulation. The simulation model was established referring to⁶⁶ and the geometry and other settings of the model are specified below. The geometry is one-dimensional and consists of 2 domains, the surfactant layer and the solution layer. According to our experiment, the thickness of the surfactant layer is 22.1 μm . Supplementary Fig. 36 shows the governing equations and boundary conditions, as well as a list of all parameters and coefficients used in the simulations. The governing equation for transportation is:

$$\nabla \bullet J_i = R_i \quad (18)$$

where the ∇ operator stands for d/dx , J_i is the flux and R_i is the production rate of the species. J_i is given by:

$$J_i = -D_i \nabla C_i - z_i F C_i \frac{D_i}{RT} \nabla \varphi \quad (19)$$

In this equation, D_i , C_i , and z_i are the diffusion coefficient, concentration, and charge of ion species, respectively. φ is the potential, F is the Faradaic constant, and u is the velocity of the solvent. The diffusion coefficients in the surfactant layer were set to 1/10 of the values in water (the solution layer) for each species.

The electric charge distribution was assumed to be uniform in the surfactant layer and the value was set -100 C cm^{-3} to $+20014 \text{ C cm}^{-3}$ according to the estimate.

The reversible reaction between H^+ and OH^- was considered in the simulation:



where k_{w1} is the rate constant of water dissociation, k_{w2} is the rate constant of neutralization reaction. Thus, the R is given by:

$$R_{\text{SO}_4^{2-}} = 0 \quad (21)$$

$$R_{\text{H}^+} = R_{\text{OH}^-} = k_{w1} - k_{w2} C_{\text{H}^+} + C_{\text{OH}^-} \quad (22)$$

OHP is defined as the origin of x axis. The left boundary condition ($x=0$) of the Nernst Planck equation is the flux J_i , which is built in COMSOL using the Flux/Source boundary. J_i is given by:

$$J_{\text{SO}_4^{2-}, x=0} = J_{\text{OH}^-, x=0} \quad (23)$$

For specie H^+ , J_i is given by:

$$J_{\text{H}^+} = -A \gamma_{\text{H}^+} \beta C_{\text{H}^+} \exp\left[-\frac{F\beta(\varphi_M - \varphi_{x=0})}{RT}\right] \quad (24)$$

β is the transfer coefficient, γ_{H^+} is the activity coefficient of H^+ .

The right boundary ($x=L_{\text{tot}}$) condition is the concentrations of species in bulk solution, which is given by:

$$C_{\text{H}^+, x=L_{\text{tot}}} = 0.1 \text{ M} \quad (25)$$

$$C_{\text{OH}^-, x=L_{\text{tot}}} = 10^{-13} \quad (26)$$

$$C_{\text{SO}_4^{2-}, x=L_{\text{tot}}} = 0.05 \text{ M} \quad (27)$$

The Poisson equation is utilized to model the electric field generated from the charged species. The Poisson equation is given by:

$$(\varepsilon_r \varepsilon_0) \nabla^2 \varphi = \rho_v + F \sum z_i C_i \quad (28)$$

In the above equation, ρ_v is the charge density carried by the surfactant layer, which is 0 outside the layer. ε_0 is the permittivity of vacuum and ε_r is the relative permittivity. The left boundary ($x=0$) condition of Poisson equation is the surface excess charge density of the cathode, which is built in COMSOL using the Flux/Source boundary. The surface charge density of the cathode σ is given by:

$$\sigma = -\varepsilon_0 \varepsilon_r \frac{\varphi_{x=0} - \varphi_M}{d} \quad (29)$$

where $\varphi_{x=0}$ is the potential at OHP, φ_M is the potential at electrode, d is the thickness of Stern layer, which was set to 0.4 nm.

The right boundary ($x=L_{\text{tot}}$) is the potential of bulk solution, which is given by:

$$\Phi_{x=L_{\text{tot}}} = 0 \text{ V} \quad (30)$$

All potential values used in the simulation is on the point of zero charge (PZC) scale.

Potential conversion from gold PZC to RHE

The potential values used in the simulations are referenced to the PZC of gold. In acidic solutions, the PZC of gold is approximately 0.20 V versus the standard hydrogen electrode (SHE). To convert these potential values from the PZC reference to the SHE scale, we apply the following relation: $\varphi_{\text{SHE}} = \varphi_{\text{PZC}} - 0.20 \text{ V}$. Subsequently, the potentials are converted from the SHE to the RHE scale using the established relationship in acidic media: $\varphi_{\text{RHE}} = \varphi_{\text{SHE}} + 0.0591 \times \text{pH}$.

DFT calculations for valence band and thermodynamic energy barrier

DFT simulations were performed using the Vienna Ab initio Simulation Package (VASP) within a plane-wave basis framework and the projector augmented wave (PAW) method. The exchange–correlation energy was described by the Perdew–Burke–Ernzerhof (PBE) functional under the generalized gradient approximation (GGA) scheme. A kinetic energy cutoff of 520 eV was applied for the plane-wave expansion. The Brillouin zone was sampled with Γ -centered k-point meshes generated automatically by VASP, using a grid density of $3 \times 3 \times 1$ for the Au(111) slab and $2 \times 2 \times 1$ for the stepped Au(211) surface. All atomic positions were optimized until the maximum residual force on each atom was below 0.01 eV \AA^{-1} , and the total energy convergence criterion was set to 10^{-5} eV . Electronic occupations were treated with Gaussian smearing of 0.05 eV, and dispersion interactions were corrected using the DFT-D3 scheme of Grimme. For calculations involving an external electric field, a field strength was applied along the surface normal to simulate the interfacial electrochemical environment. The Gibbs free energy change (ΔG) of each elementary step was evaluated using the computational hydrogen electrode model:

$$\Delta G = \Delta E_{\text{DFT}} + \Delta E_{\text{ZPE}} - T\Delta S + \Delta G_{\text{U}} \quad (31)$$

where ΔE_{DFT} , ΔE_{ZPE} , and ΔS represent the total electronic energy, zero-point energy, and entropy change, respectively. $\Delta G_{\text{U}} = -n_e U$ accounts for the effect of the applied potential U relative to the standard hydrogen electrode (SHE), with n_e being the number of transferred electrons.

Overpotential reduction calculation

The reduction in overpotential (ΔE) was calculated from the corresponding free energy change (ΔG) using the thermodynamic relationship:

$$\Delta E = \frac{\Delta G}{nF} \quad (32)$$

where n is the number of electrons transferred in the rate-determining step ($n=1$) and F is the Faraday constant (96485 C mol^{-1}).

Molecular dynamics simulations

We have investigated the diffusion process of proton and CO_2 towards an Au surface that is coated with adsorption layers of CTAC, PVP, and SDS, respectively, using molecular dynamics simulations. Three models, Au/CTAC, Au/PVP, and Au/SDS were built. In each model, the Au surface was in contact with the modification layer and the solution. The Au surface model (1152 Au atoms) was constructed by cleaving a bulk Au crystal along (111) plane to create a 6-layer slab with XY interface area of $34.61 \times 39.96 \text{ \AA}^2$. The CTAC and SDS layers were prepared by placing 48 molecules on the Au slab, respectively, while PVP layer was represented by 24 10-unit PVP oligomers. Due to the inability of non-reactive force fields to capture the dynamic nature of proton hopping, we have chosen to represent protons explicitly as H^+ ions in our simulations. For Solution/PVP/Au model, the solution included 100 H^+ , 50 SO_4^{2-} , 50 CO_2 , and 4000 H_2O molecules. For Solution/CTAC/Au and Solution/SDS/Au, 48 Cl^- and 48 Na^+ counter ions were also added to the solution maintain electrical neutrality. Each model had a Z direction length of 200 \AA , leaving a vacuum layer exceeding 50 \AA to minimize periodic image interactions.

In each case, at the beginning of the simulation, energy of the model system was minimized to eliminate the steric overlap and correct any inappropriate geometries. This was followed by a 7.0 ns NVT molecular dynamics simulation at a constant temperature of 298 K to

track system dynamics. The two bottommost Au layers were held fixed during all simulations. An electric field of -0.012 V/\AA , oriented along the Z direction, was applied.

LAMMPS⁷⁷ and PCFF-INTERFACE force field⁷⁸ were used to perform the molecular simulations. A cutoff of 1.2 nm was employed to capture van der Waals and short-range electrostatic interactions in the systems, and the PPPM method with a relative precision of 10^{-5} was used to account for the long-range electrostatic interactions⁷⁹. During the molecular dynamics simulations, a time step of 1.0 fs was used, and the temperature was controlled by the Nosé–Hoover thermostat⁸⁰. Equations of motions were integrated using the Verlet velocity method.

Data availability

The authors declare that the data supporting the findings of this study are available within the paper and its Supplementary Information files. Schematic diagrams are provided for Fig. 1 in the paper. Source data for Figs. 2–5 and Supplementary Figs. are included with this paper. Additional data are available from the corresponding author upon request. Source data are provided with this paper.

References

- Seh, Z. W. et al. Combining theory and experiment in electrocatalysis: insights into materials design. *Science* **355**, eaad4998 (2017).
- Lees, E. W., Mowbray, B. A. W., Parlange, F. G. L. & Berlinguette, C. P. Gas diffusion electrodes and membranes for CO_2 reduction electrolyzers. *Nat. Rev. Mater.* **7**, 55–64 (2022).
- Rabinowitz, J. A. & Kanan, M. W. The future of low-temperature carbon dioxide electrolysis depends on solving one basic problem. *Nat. Commun.* **11**, 5231 (2020).
- Zhang, B. A., Ozel, T., Elias, J. S., Costentin, C. & Nocera, D. G. Interplay of homogeneous reactions, mass transport, and kinetics in determining selectivity of the reduction of CO_2 on gold electrodes. *ACS Cent. Sci.* **5**, 1097–1105 (2019).
- Chen, C., Li, Y. & Yang, P. Address the “alkalinity problem” in CO_2 electrolysis with catalyst design and translation. *Joule* **5**, 737–742 (2021).
- Ozden, A. et al. Cascade CO_2 electroreduction enables efficient carbonate-free production of ethylene. *Joule* **5**, 706–719 (2021).
- Ma, M. et al. Insights into the carbon balance for CO_2 electroreduction on Cu using gas diffusion electrode reactor designs. *Energy Environ. Sci.* **13**, 977–985 (2020).
- O’Brien, C. P. et al. Single pass CO_2 conversion exceeding 85% in the electro-synthesis of multicarbon products via local CO_2 regeneration. *ACS Energy Lett.* **6**, 2952–2959 (2021).
- Gu, J. et al. Modulating electric field distribution by alkali cations for CO_2 electroreduction in strongly acidic medium. *Nat. Catal.* **5**, 268–276 (2022).
- Bondue, C. J., Graf, M., Goyal, A. & Koper, M. T. M. Suppression of hydrogen evolution in acidic electrolytes by electrochemical CO_2 reduction. *J. Am. Chem. Soc.* **143**, 279–285 (2021).
- Huang, J. E. et al. CO_2 electrolysis to multicarbon products in strong acid. *Science* **372**, 1074–1078 (2021).
- Monteiro, M. C. O., Philips, M. F., Schouten, K. J. P. & Koper, M. T. M. Efficiency and selectivity of CO_2 reduction to CO on gold gas diffusion electrodes in acidic media. *Nat. Commun.* **12**, 4943 (2021).
- Xie, Y. et al. High carbon utilization in CO_2 reduction to multi-carbon products in acidic media. *Nat. Catal.* **5**, 564–570 (2022).
- Ma, Z. et al. CO_2 electroreduction to multicarbon products in strongly acidic electrolyte via synergistically modulating the local microenvironment. *Nat. Commun.* **13**, 7596 (2022).
- Pan, B. et al. Close to 90% single-pass conversion efficiency for CO_2 electroreduction in an acid-fed membrane electrode assembly. *ACS Energy Lett.* **7**, 4224–4231 (2022).

16. Zhao, Y. et al. Conversion of CO₂ to multicarbon products in strong acid by controlling the catalyst microenvironment. *Nat. Synth.* **2**, 403–412 (2023).
17. Li, H. et al. Tailoring acidic microenvironments for carbon-efficient CO₂ electrolysis over Ni-N-C catalyst in a membrane electrode assembly electrolyzer. *Energy Environ. Sci.* **16**, 1502–1510 (2023).
18. Nie, W., Heim, G. P., Watkins, N. B., Agapie, T. & Peters, J. C. Organic additive-derived films on Cu electrodes promote electrochemical CO₂ reduction to C₂₊ products under strongly acidic conditions. *Angew. Chem. Int. Ed.* **62**, e202216102 (2023).
19. Qin, H.-G. et al. Quantitative understanding of cation effects on the electrochemical reduction of CO₂ and H⁺ in acidic solution. *ACS Catal.* **13**, 916–926 (2023).
20. Zi, X. et al. Breaking K⁺ concentration limit on Cu nanoneedles for acidic electrocatalytic CO₂ reduction to multi-carbon products. *Angew. Chem. Int. Ed.* **62**, e202309351 (2023).
21. Moss, A. B. et al. In operando investigations of oscillatory water and carbonate effects in MEA-based CO₂ electrolysis devices. *Joule* **7**, 350–365 (2023).
22. Bui, J. C. et al. Engineering catalyst–electrolyte microenvironments to optimize the activity and selectivity for the electrochemical reduction of CO₂ on Cu and Ag. *Acc. Chem. Res.* **55**, 484–494 (2022).
23. Verma, S. et al. Insights into the low overpotential electroreduction of CO₂ to CO on a supported gold catalyst in an alkaline flow electrolyzer. *ACS Energy Lett.* **3**, 193–198 (2018).
24. Monteiro, M. C. O. et al. Absence of CO₂ electroreduction on copper, gold and silver electrodes without metal cations in solution. *Nat. Catal.* **4**, 654–662 (2021).
25. Monteiro, M. C. O., Dattila, F., Lopez, N. & Koper, M. T. M. The role of cation acidity on the competition between hydrogen evolution and CO₂ reduction on gold electrodes. *J. Am. Chem. Soc.* **144**, 1589–1602 (2021).
26. Fan, M. et al. Cationic-group-functionalized electrocatalysts enable stable acidic CO₂ electrolysis. *Nat. Catal.* **6**, 763–772 (2023).
27. Tan, H. et al. Fast collective motions of backbone in transmembrane α helices are critical to water transfer of aquaporin. *Sci. Adv.* **10**, eade9520 (2024).
28. Roy, A. et al. Foldamer-based ultrapermeable and highly selective artificial water channels that exclude protons. *Nat. Nanotechnol.* **16**, 911–917 (2021).
29. Ma, Z., Yin, H., Lyu, P. & Xu, Y. Protruding-shaped Co polarization field on ultrathin covalent triazine framework nanosheets for efficient CO₂ photoreduction. *Adv. Energy Mater.* **14**, 2401619 (2024).
30. Zhou, M. et al. Construction of frustrated Lewis pairs in poly(-heptazine imide) nanosheets via hydrogen bonds for boosting CO₂ photoreduction. *Angew. Chem. Int. Ed.* **63**, e202407468 (2024).
31. Zhao, W. & Wang, T. Revisiting factors controlling the electrochemical CO₂ reduction to CO and HCOOH on transition metals with grand canonical density functional theory calculations. *ACS Catal.* **14**, 8549–8560 (2024).
32. Ringe, S. et al. Double layer charging driven carbon dioxide adsorption limits the rate of electrochemical carbon dioxide reduction on gold. *Nat. Commun.* **11**, 33 (2020).
33. Beil, R. L. & Hinde, R. J. Ab initio electrical properties of CO₂: polarizabilities, hyperpolarizabilities, and multipole moments. *Theor. Chem. Acc.* **140**, 120 (2021).
34. Li, Z. et al. Dipole field in nitrogen-enriched carbon nitride with external forces to boost the artificial photosynthesis of hydrogen peroxide. *Nat. Commun.* **14**, 5742 (2023).
35. Liu, P. et al. Tip-enhanced electric field: a new mechanism promoting mass transfer in oxygen evolution reactions. *Adv. Mater.* **33**, 2007377 (2021).
36. Zhou, K. & Li, L. Nanotip-induced electric field for electrocatalysis. *J. Alloy. Compd.* **1002**, 175549 (2024).
37. Li, J. et al. Accelerated dinitrogen electroreduction to ammonia via interfacial polarization triggered by single-atom protrusions. *Chem* **6**, 885–901 (2020).
38. Liu, M. et al. Enhanced electrocatalytic CO₂ reduction via field-induced reagent concentration. *Nature* **537**, 382–386 (2016).
39. Li, J. et al. Hollow hierarchical Cu₂O-derived electrocatalysts steering CO₂ reduction to multi-carbon chemicals at low overpotentials. *Adv. Mater.* **35**, 2301127 (2023).
40. Pan, X. et al. Electric-field-assisted proton coupling enhanced oxygen evolution reaction. *Nat. Commun.* **15**, 3354 (2024).
41. Chen, L.-W. et al. Multi-twinned gold nanoparticles with tensile surface steps for efficient electrocatalytic CO₂ reduction. *Sci. China Chem.* **65**, 2188–2196 (2022).
42. Yang, P.-P. & Gao, M.-R. Enrichment of reactants and intermediates for electrocatalytic CO₂ reduction. *Chem. Soc. Rev.* **52**, 4343–4380 (2023).
43. Yin, J. et al. The built-in electric field across FeN/Fe₃N interface for efficient electrochemical reduction of CO₂ to CO. *Nat. Commun.* **14**, 1724 (2023).
44. Shen, M. et al. Hierarchical design enables sufficient activated CO₂ for efficient electrolysis of bicarbonate to CO. *Joule* **8**, 1999–2015 (2024).
45. Shi, C., Hansen, H. A., Lausche, A. C. & Nørskov, J. K. Trends in electrochemical CO₂ reduction activity for open and close-packed metal surfaces. *Phys. Chem. Chem. Phys.* **16**, 4720–4727 (2014).
46. Vijay, S. et al. Unified mechanistic understanding of CO₂ reduction to CO on transition metal and single atom catalysts. *Nat. Catal.* **4**, 1024–1031 (2021).
47. Domínguez-Flores, F. & Melander, M. M. Approximating constant potential DFT with canonical DFT and electrostatic corrections. *J. Chem. Phys.* **158**, 144701 (2023).
48. Ringe, S. The importance of a charge transfer descriptor for screening potential CO₂ reduction electrocatalysts. *Nat. Commun.* **14**, 2598 (2023).
49. Chen, L. et al. High-yield seedless synthesis of triangular gold nanoplates through oxidative etching. *Nano Lett.* **14**, 7201–7206 (2014).
50. Scarabelli, L., Coronado-Puchau, M., Giner-Casares, J. J., Langer, J. & Liz-Marzán, L. M. Monodisperse gold nanotriangles: size control, large-scale self-assembly, and performance in surface-enhanced Raman scattering. *ACS Nano* **8**, 5833–5842 (2014).
51. Gómez-Graña, S. et al. Surfactant (bi)layers on gold nanorods. *Langmuir* **28**, 1453–1459 (2012).
52. O'Brien, M. N., Jones, M. R., Kohlstedt, K. L., Schatz, G. C. & Mirkin, C. A. Uniform circular disks with synthetically tailorable diameters: two-dimensional nanoparticles for plasmonics. *Nano Lett.* **15**, 1012–1017 (2015).
53. Chen, H. et al. Plasmon coupling in clusters composed of two-dimensionally ordered gold nanocubes. *Small* **5**, 2111–2119 (2009).
54. Limaye, A. M., Zeng, J. S., Willard, A. P. & Manthiram, K. Bayesian data analysis reveals no preference for cardinal Tafel slopes in CO₂ reduction electrocatalysis. *Nat. Commun.* **12**, 703 (2021).
55. Chen, Y., Li, C. W. & Kanan, M. W. Aqueous CO₂ reduction at very low overpotential on oxide-derived Au nanoparticles. *J. Am. Chem. Soc.* **134**, 19969–19972 (2012).
56. Limaye, M., Zeng, J. S., Willard, A. P. & Manthiram, K. Bayesian data analysis reveals no preference for cardinal Tafel slopes in CO₂ reduction electrocatalysis. *Nat. Commun.* **12**, 703 (2021).
57. Qin, X., Hansen, H. A., Honkala, K. & Melander, M. M. Cation-induced changes in the inner- and outer-sphere mechanisms of electrocatalytic CO₂ reduction. *Nat. Commun.* **14**, 7607 (2023).
58. Banerjee, S., Han, X. & Thoi, V. S. Modulating the electrode–electrolyte interface with cationic surfactants in carbon dioxide reduction. *ACS Catal.* **9**, 5631–5637 (2019).

59. Banerjee, S., Zhang, Z.-Q., Hall, A. S. & Thoi, V. S. Surfactant perturbation of cation interactions at the electrode–electrolyte interface in carbon dioxide reduction. *ACS Catal.* **10**, 9907–9914 (2020).
60. Adler, Z. et al. Hydrogen peroxide electrosynthesis in a strong acidic environment using cationic surfactants. *Precis. Chem.* **2**, 129–137 (2024).
61. Pan, H., Wang, F., Zhang, Z. & Min, S. Interfacial modification of Zn foil electrode with cationic surfactants enables efficient and selective CO production from CO₂ electroreduction. *Sustain. Energ. Fuels* **6**, 2149 (2022).
62. Zhang, X. et al. Selective and efficient CO₂ electroreduction to formate on copper electrodes modified by cationic gemini surfactants. *Angew. Chem. Int. Ed.* **63**, e202315822 (2024).
63. Jakobsen, J. B., Rønne, M. H., Daasbjerg, K. & Skrydstrup, T. Are amines the holy grail for facilitating CO₂ reduction?. *Angew. Chem. Int. Ed.* **60**, 9174–9179 (2021).
64. Bai, J., Wang, W. & Liu, J. Bioinspired hydrophobicity for enhancing electrochemical CO₂ reduction. *Chem. Eur. J.* **29**, e202302461 (2023).
65. Yang, X. et al. Cation-induced interfacial hydrophobic micro-environment promotes the C–C coupling in electrochemical CO₂ reduction. *J. Am. Chem. Soc.* **146**, 5532–5542 (2024).
66. Qin, H.-G. et al. Surface-immobilized cross-linked cationic poly-electrolyte enables CO₂ reduction with metal cation-free acidic electrolyte. *Nat. Commun.* **14**, 5640 (2023).
67. Mayer, M. et al. Controlled living nanowire growth: precise control over the morphology and optical properties of AgAuAg bimetallic nanowires. *Nano Lett.* **15**, 5427–5437 (2015).
68. Scarabelli, L., Grzelczak, M. & Liz-Marzán, L. M. Tuning gold nanorod synthesis through prereduction with salicylic acid. *Chem. Mater.* **25**, 4232–4238 (2013).
69. Rodríguez-Fernández, J., Pérez-Juste, J., Mulvaney, P. & Liz-Marzán, L. M. Spatially-directed oxidation of gold nanoparticles by Au(III)–CTAB complexes. *J. Phys. Chem. B* **109**, 14257–14261 (2005).
70. Gabardo, C. M. et al. Combined high alkalinity and pressurization enable efficient CO₂ electroreduction to CO. *Energy Environ. Sci.* **11**, 2531–2539 (2018).
71. Frisch, M. et al. *Gaussian 16, Revision C. 01 Normal Name Order* (Gaussian, 2016).
72. Stephens, P. J., Devlin, F. J., Chabalowski, C. F. & Frisch, M. J. Ab initio calculation of vibrational absorption and circular dichroism spectra using density functional force fields. *J. Phys. Chem.* **98**, 11623–11627 (1994).
73. Lu, T. & Chen, Q. Ultrastrong regulation effect of the electric field on the all-carboatomic ring cyclo[18]carbon. *ChemPhysChem* **22**, 386–395 (2021).
74. Lu, T. & Chen, F. Multiwfn: a multifunctional wavefunction analyzer. *J. Comput. Chem.* **33**, 580–592 (2012).
75. Humphrey, W., Dalke, A. & Schulten, K. VMD: visual molecular dynamics. *J. Mol. Graph.* **14**, 33–38 (1996).
76. Liu, W. et al. Industrial-level modulation of catalyst–electrolyte microenvironment for electrocatalytic CO₂ reduction: challenges and advancements. *Adv. Energy Mater.* **14**, 2402942 (2024).
77. Plimpton, S. Fast parallel algorithms for short-range molecular dynamics. *J. Comput. Phys.* **117**, 1–19 (1995).
78. Heinz, H., Lin, T.-J., Mishra, R. K. & Emami, F. S. Thermodynamically consistent force fields for the assembly of inorganic, organic, and biological nanostructures: the interface force field. *Langmuir* **29**, 1754–1765 (2013).
79. Liu, W. et al. Nitrogen-rich porous-conjugated framework for efficient capture and electroreduction of simulated flue gas in acidic electrolyte. *J. Am. Chem. Soc.* **147**, 24023–24031 (2025).
80. Nosé, S. Constant temperature molecular dynamics methods. *Prog. Theor. Phys. Supp.* **103**, 1–46 (1991).

Acknowledgements

This work is supported by Shandong Provincial Natural Science Foundation (No. ZR2024QB122); National Key Research and Development Program of China (No. 2020YFB1506300, 2023YFB3810002); National Natural Science Foundation of China (Nos. 22405069, 22375017, U22A20348, U21A20377); and Research Program of Qilu Institute of Technology (No. QIT23TP011). The authors thank the Analysis and Testing Center of BIT and QIT, as well as Shiyanjia Lab (www.shiyanjia.com) and Ceshigo (www.ceshigo.com), for technical support.

Author contributions

L.W.C., Y.C.H., B.W., and J.B.S. designed the research. L.W.C., Z.B.G., and Y.C.H. performed the catalyst preparation, characterization, photocatalytic tests, and data analysis. H.Z.H., W.J.T., X.X.C., Q.H., D.L., C.S., M.M.G., S.Q.H., S.H.L., H.Q.Z., and L.Y.H. assisted with the material synthesis, characterizations, and catalysis measurements. L.W.C., Y.C.H., B.W., and J.B.S. wrote the paper. L.Y.H., H.Y.M., X.G., Y.C.H., W.X.Y., Q.S.L., B.W., and J.B.S. supervised the research. All authors discussed the results and assisted during manuscript preparation.

Competing interests

The authors declare no competing interests.

Additional information

Supplementary information The online version contains supplementary material available at <https://doi.org/10.1038/s41467-026-68435-y>.

Correspondence and requests for materials should be addressed to Liwei Chen, Yuchen Hao, Qunsheng Li, Bo Wang or Jibin Song.

Peer review information *Nature Communications* thanks Devis Di Tommaso, and the other anonymous, reviewer(s) for their contribution to the peer review of this work. A peer review file is available.

Reprints and permissions information is available at <http://www.nature.com/reprints>

Publisher's note Springer Nature remains neutral with regard to jurisdictional claims in published maps and institutional affiliations.

Open Access This article is licensed under a Creative Commons Attribution-NonCommercial-NoDerivatives 4.0 International License, which permits any non-commercial use, sharing, distribution and reproduction in any medium or format, as long as you give appropriate credit to the original author(s) and the source, provide a link to the Creative Commons licence, and indicate if you modified the licensed material. You do not have permission under this licence to share adapted material derived from this article or parts of it. The images or other third party material in this article are included in the article's Creative Commons licence, unless indicated otherwise in a credit line to the material. If material is not included in the article's Creative Commons licence and your intended use is not permitted by statutory regulation or exceeds the permitted use, you will need to obtain permission directly from the copyright holder. To view a copy of this licence, visit <http://creativecommons.org/licenses/by-nc-nd/4.0/>.

© The Author(s) 2026